Journal of Manufacturing Processes 151 (2025) 354–371

Contents lists available at ScienceDirect

Journal of Manufacturing Processes

journal homepage: www.elsevier.com/locate/manpro

Data-driven optimization of laser scanning conditions in laser powder bed fusion for defect-free IN738LC components

Masahiro Kusano [a,*], Toshio Osada [a], Makoto Watanabe [a]

[a] Research Center for Structural Materials, National Institute for Materials Science, 1-2-1 Sengen, Tsukuba 305-0047, Ibaraki, Japan

ARTICLE INFO

Keywords:
Laser powder bed fusion
Inconel 738 LC
Solidification cracking
electron backscatter diffraction
Causal analysis

ABSTRACT

Manufacturing defect-free superalloy components using laser powder bed fusion (L-PBF) remains a challenging and urgent issue due to the high susceptibility of the process to microcracking. While previous studies have investigated how individual laser scanning parameters influence microcracking behavior in superalloy components, a comprehensive process window for crack density has yet to be developed. Moreover, the relationship between laser scanning conditions and crack density is often treated as a black-box model, without explicitly considering the underlying fundamental mechanisms. Thus, the purpose of this study is twofold: first, to establish a comprehensive process window for crack density in order to fabricate defect-free IN738LC components by L-PBF; and second, to elucidate the fundamental mechanisms linking laser scanning conditions to solidification cracking through empirical causal analysis based on microstructural features. To this end, more than 100 sets of laser scanning conditions were investigated, and the optimal conditions were found to minimize the defect ratio and crack density to <0.060 % and 0.005 mm/mm^2, respectively. The suitability was further validated by fabricating turbine-blade shaped parts without internal defects. Then, microstructural features for all samples were extracted using electron backscatter diffraction, and the resulting dataset was used to develop regression models for predicting crack density. The multiple linear regression and support vector regression models revealed that two common key microstructural features—grain refinement and the alignment of ⟨001⟩ to the building direction—play a primary role in suppressing microcracking. On the other hand, the findings also imply that incorporating additional metallurgical and mechanical features may be essential for enhancing the predictive performance.

1. Introduction

The nickel-based superalloy Inconel738LC (IN738LC) with γ-γ′ two phase structure was designed to have excellent high-temperature creep property with corrosion resistance, and is extensively used as blades for gas turbine engines. Conventionally, such engine components with complex geometry have been manufactured by precision casting, but metal additive manufacturing (AM) has the potential to replace this approach. Powder bed fusion (PBF), one of the AM methods, can fabricate near-net shape products with high dimensional accuracy by alternately spreading raw powder on a platform and selectively irradiating a heat source to melt and solidify it. A focused laser or electron beam is used as the heat source, and the process is referred to as laser powder bed fusion (L-PBF) or electron beam powder bed fusion (EB-PBF). One of the advantages of manufacturing such gas turbine engine components by PBF is the design flexibility to integrate multiple components into one (part consolidation) and form internal cooling structures. Indeed, Solar Turbines Inc. [1] has actually tried to fabricate IN738LC turbine blades using EB-PBF.

Despite such successful demonstrations of the manufacture of IN738LC products using PBF, one of the challenges for practical application is the propensity for microcracking during the process. Such cracking has also been a longstanding problem in the welding field, and its mechanism is well understood based on extensive experimental and numerical studies [2–6]. According to these studies, solidification cracking occurs during the terminal stages of solidification when liquid films are distributed along solidification grain boundaries. Such grain boundaries with a continuous liquid film cannot withstand the tensile strain due to thermal contraction and solidification shrinkage, resulting in microcracking. Considering these mechanisms, several simplified indices as criteria for susceptibility to solidification cracking have been proposed [7–9]. In the comprehensive study by Ghoussoub et al. [9], the

* Corresponding author.
E-mail address: KUSANO.Masahiro@nims.go.jp (M. Kusano).

https://doi.org/10.1016/j.jmapro.2025.07.023
Received 20 January 2025; Received in revised form 6 June 2025; Accepted 6 July 2025

indices for IN738LC were found to be relatively higher than those of IN718 and IN625, and comparable to those for IN939 and CM247LC. This trend was consistent with the experimental observations of samples fabricated by L-PBF. Recently, several groups have sought to clarify the mechanisms underlying liquid film formation at the grain boundaries by simulating dendrite growth during solidification in the AM processes using the phase field method [10–12]. According to these studies, the dendrite spacing (the liquid channel) at the grain boundaries increases in convergent rather than divergent grain boundaries and with larger misorientations, causing hot cracking.

Metallurgical factors, including microsegregation and secondary phase precipitation, also affect the susceptibility of components to solidification cracking. In the case of IN738LC parts fabricated by PBF, segregation of minor impurities [13–17] and precipitation of carbides [13,14,18] and oxides [19,20] have also been observed on the cracked fracture surface. Detailed observations of IN738LC L-PBF samples by Hariharan et al. [16] using atom probe tomography coupled with transmission Kikuchi diffraction showed enrichment of boron and carbon at both the high and low angle grain boundaries (HAGBs and LAGBs), whereas zirconium and silicon enrichment were only observed at HAGBs. In addition, their diffusion calculations suggested that such chemical profiles can be attributed to both microsegregation during solidification and solid-state segregation during cooling. To suppress segregation and precipitation at the grain boundaries, it was effective to lower the content of grain boundary strengthening elements such as carbon [13] and zirconium [14,16], and impurities such as silicon [16,20] and manganese [20] in the alloy composition of IN738LC, resulting in less microcracking. Instead of lowering these elements, Zhou et al. [21] reported that the addition of TiC nanoparticles to the raw IN738LC powder yielded more tortuous HAGBs, which alleviated solute enrichment and strain concentration, reducing the crack density from 0.64 mm/mm^2 to 0.02 mm/mm^2. The effect on cracking susceptibility according to such alloy composition, precipitates, and microsegregation has also been studied in other nickel-base alloys such as IN625 [22], René 104 [23], and Hastelloy X [24]. According to the study by Benoit et al. [22], although the composition of powder was within the standard range of IN625, samples fabricated from powder with increased silicon and niobium content exhibited significantly more solidification cracking compared to those built from powder with lower levels of these elements. In René 104, the addition of scandium and yttrium led to the precipitation of nano-Al_3(Sc, Y) phases during solidification, refining both the grain and cellular structures [23]. This facilitated the formation of equiaxed grains instead of columnar ones, effectively inhibiting solidification cracking. Tomus et al. [24] suggested that Hastelloy X was also susceptible to cracking at high silicon and carbon contents in the composition due to the precipitated carbides along grain boundaries.

As for mechanical factors, solidification cracking in welding is more likely to occur when the thermal expansion coefficient or solidification shrinkage of the material is higher, or when the workpiece is more constrained [2,4]. In terms of such mechanical factors, Kitano et al. [25] conducted a finite element thermal elastoplastic analysis to simulate the plastic strain evolution during solidification. They determined the critical plastic strain increment for solidification cracking by correlating their simulation results with experimental observations from bead-on-plate tests of laser scanning on a Hastelloy X plate. Similarly, Kadoi et al. [26] reproduced solidification cracking in as-fabricated IN718 by conducting bead-on-plate tests under horizontal tensile loading and quantitatively evaluated the critical strain rate as a criterion for crack initiation. An effective way to reduce the strain during solidification is preheating of the workpiece, and indeed, solidification cracking in welding of steel and aluminum alloys could be suppressed by proper preheating [4]. Chen et al. [18] have successfully manufactured crack-free IN738LC by the L-PBF process by preheating the platform to 700 °C, although they concluded that the reduction of hot cracking was attributable to the smaller number of HAGBs and lower cooling rate due to preheating rather than to lower strain. As for EB-PBF, preheating is usually necessary to prevent powder repulsion caused by the accumulation of electrons (the so-called “smoking effect” [27,28]). Li et al. [29] fabricated crack-free IN738LC samples by EB-PBF with the substrate heated up to 1070 °C. In our previous study [30], we deliberately induced heat accumulation in IN738LC samples during the L-PBF process by designing a constricted sample geometry and setting a shorter time per layer (*TPL*). The sample temperature was held above 600 °C throughout the process without any preheating system, but contrary to our expectations, more severe solidification cracks were found in such heat-accumulated samples. Although it seems to contradict the above mechanism to reduce cracking by preheating, cooling the area behind the weld pool to increase the cooling rate is also effective to avoid solidification cracking [2]. This can be explained by the theory that increasing the cooling rate dT/dt lowers the critical strain value ($d\varepsilon/dT = (d\varepsilon/dt)/(dT/dt)$) in the brittle temperature range (BTR) below a threshold for solidification cracking. Therefore, a complex combination of metallurgical and mechanical factors can cause microcracking in the welding and PBF processes.

Furthermore, microcracking in PBF is more intricate than that in welding because of the cyclic thermal history and iterative melting and solidification caused by track-by-track and layer-by-layer heat source scanning. To date, several experimental studies have attempted to reduce cracking of IN738LC during L-PBF by changing the laser power P, scanning velocity v, hatching space h, and scanning strategies. Volumetric and linear energy densities (defined as P/vhd and P/v, respectively; d refers to powder layer thickness) are often used as an indicator to maximize the sample density by avoiding both spherical pores due to keyholing and irregularly shaped crevices due to lack of fusion (LOF). While Cloots et al. [17] concluded that the crack density can only be reduced with a compromise in such porosity, other studies have experimentally determined energy densities that reduce both microcracking and porosity for IN738LC [13,18,19,31–34]. Grange et al. [32] calculated the single-track temperature field with different laser powers and scanning velocities by using an analytical solution, and found that the larger the melt pool, the larger the crack density. In addition, they revealed that overlapping adjacent melt pools with narrow hatching space minimized microcracking, which was attributed to a partial repair of cracks by remelting. In addition, the scanning strategy also seems to be an important factor in reducing the cracking of IN738LC components [15,35,36]. These studies [15,36] reported that samples fabricated with different rotation angles of the meander scanning pattern exhibited lower crack density at 90° than at 0°, and the lowest at 67°. According to Xu et al. [15], grain refinement and the reduction of residual stress due to the scanning strategy contributed to the inhibition of initiation and propagation of cracks. Nevertheless, while previous studies have investigated how individual laser scanning parameters influence microcracking behavior in IN738LC components, a comprehensive process window that quantitatively incorporates relationships between all the above primary parameters including hatching space and crack density has yet to be developed. Such a process window clearly identifies the optimal laser scanning conditions minimizing crack density, as well as the range of parameter values that maintain the crack density below an acceptable threshold. Moreover, the relationship between laser scanning conditions and crack density can be regarded as a type of black-box model, without explicitly considering the underlying mechanisms of solidification cracking. Ideally, the causal relationship should be quantitatively interpreted using theoretical model, numerical simulations, or empirical causal analyses that take metallurgical and mechanical factors into account.

The purpose of this study is, first, to establish a comprehensive process window for crack density in the fabrication of IN738LC components by L-PBF, and to find the optimal laser scanning conditions for fabricating components without internal defects. Second, it aims to explain the fundamental mechanisms linking laser scanning conditions to solidification cracking through an empirical causal analysis considering microstructural features. To this end, more than 100 rectangular

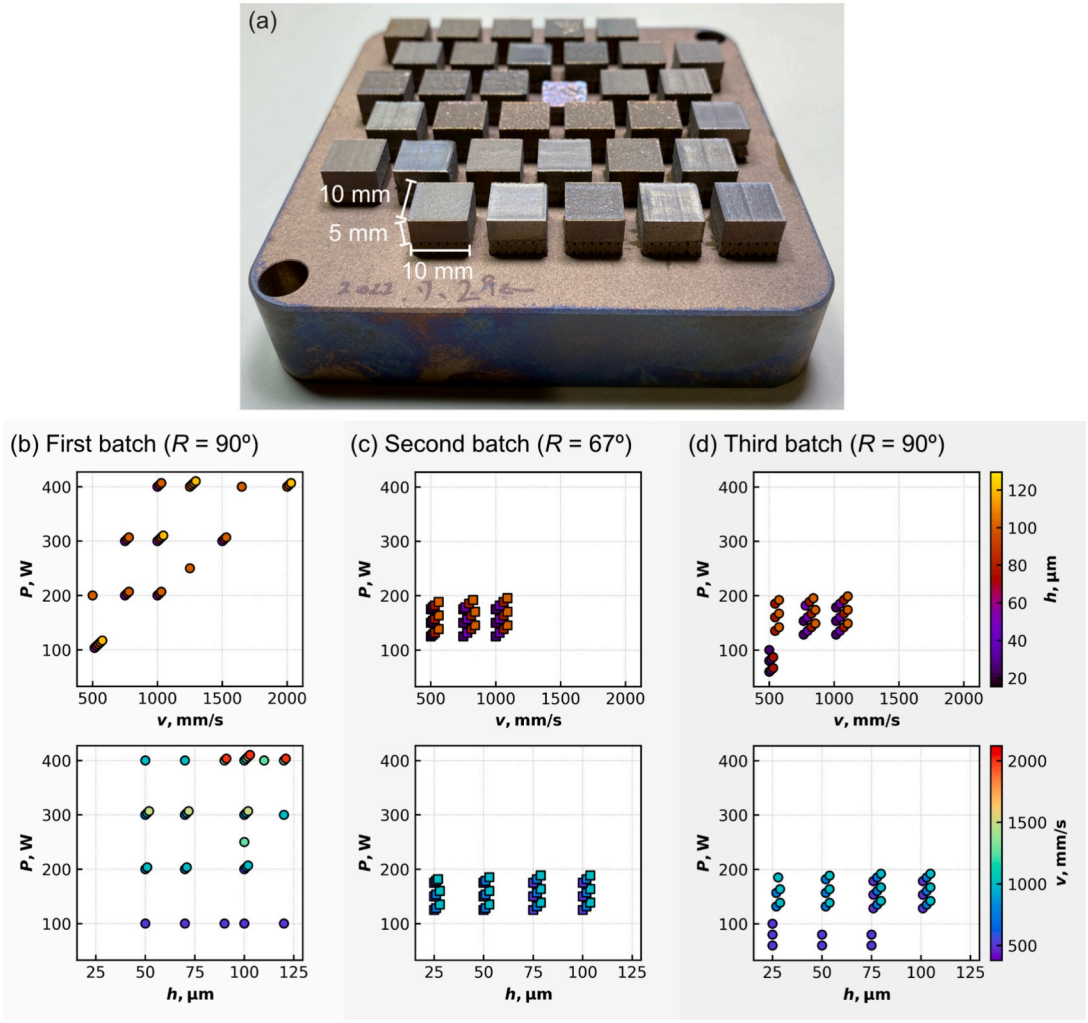

Fig. 1. (a) IN738LC cuboid samples fabricated by L-PBF, and laser scanning conditions in the (b) first, (c) second, and (d) third batches.

samples fabricated under different laser scanning conditions were analyzed. Then, the optimal conditions were applied to the fabrication of turbine blade-shaped parts to determine their suitability for manufacturing components with complex geometry (Section 3.1). The rectangle samples were further observed by electron backscatter diffraction (EBSD) to evaluate their microstructural features (Section 3.2). Based on the dataset of such microstructural features as well as the laser scanning conditions and crack density, a regression model was developed to statistically represent their relationships (Section 3.3). Finally, the results were comprehensively discussed in relation to previous experimental and simulated studies (Section 4).

2. Materials and methods

As shown in Fig. 1(a), more than 30 rectangular samples (10 mm × 10 mm × 5 mm) were fabricated on a stainless-steel baseplate by a commercial L-PBF machine (SLM280; SLM Solutions GmbH) using IN738LC powder (AMPERPRINT 0151.074; Höganäs AB). Table 1 shows the composition of the raw powder provided by the manufacturer. The samples were manufactured in three batches, with each sample within a batch subjected to different laser scanning conditions. After observing the crack density of each sample in the batch, the laser scanning conditions for the next batch were determined. The laser power P, scanning velocity v, and hatching space h for each sample were plotted in Fig. 1 (b–d), and are also summarized in Supplemental Table S1. The laser beam scanned the powder bed in a meander pattern, with the rotation angle R per layer set to 90° for the first and third batches, and 67° for the second batch, in order to investigate the effects of rotation angle as reported in references [15, 36]. At the end of each round of laser scanning, the baseplate with samples was lowered 30 µm and the powder was spread over it for the next layer. The oxygen level in the chamber was kept below 0.01 vol% by replacing the atmosphere with argon gas. Turbine blade-shaped parts were also fabricated under the optimal laser scanning conditions that minimized the defects in the rectangular samples.

The as-fabricated samples were cut and polished for microscopic observations. The horizontal cross-section (XY) near the half height was observed by an optical microscope (VHX-2000; KEYENCE Corporation), and its resolution was approximately 10 µm. To discretize the defects in the sample, the original microscopic image was binarized by using

Table 1
Chemical composition of AMPERPRINT 0151.074 (wt%, Ni = balance).

Co	Cr	Mo	W	Al	Ti	Nb	Ta	C	B	Zr	N	O	Fe	Mn	Si	P	S
8.5	15.9	1.7	2.5	3.5	3.5	0.88	1.8	0.10	0.007	0.024	0.008	0.017	0.02	0.01	0.02	0.005	0.002

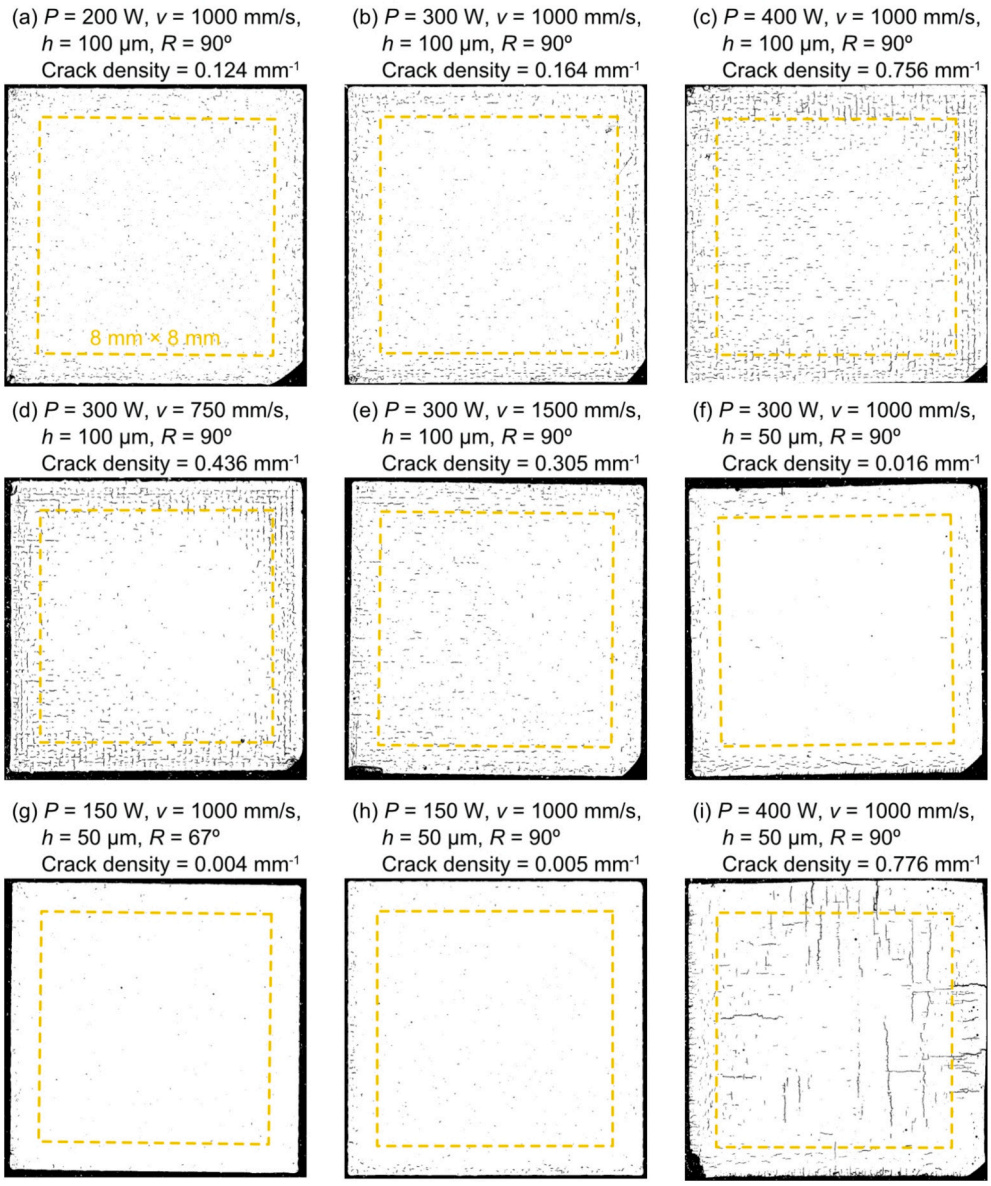

Fig. 2. Binarized optical microscope images of XY cross sections of samples built at different laser power, scanning velocity, and hatching space. The yellow dashed rectangle of 8 mm × 8 mm indicates the inside bounds of the sample. (For interpretation of the references to color in this figure legend, the reader is referred to the web version of this article.)

image analysis software (Fiji [37]). The microstructures were observed in detail by scanning electron microscopes (SEMs) (JSM-6010 LA and JSM-7200F; JEOL). The crystal orientations were characterized by an electron backscatter diffraction (EBSD) detector equipped with JSM-7200F. The accelerating voltage was set to 20 kV and the scanning step size was 1.5 μm. The measured data were analyzed with software EDAX OIM Analysis v8 to map inverse pole figure (IPF) and kernel average misorientation (KAM) and to evaluate microstructural features such as mean grain size and fraction of HAGBs. Here, the misorientation angle of HAGBs was defined as above 15°.

3. Results

3.1. Identification of the laser scanning conditions for defect-free samples

In the first batch, as shown in Fig. 1(b), IN738LC samples were built with a wide range of laser power P from 100 to 400 W, scanning velocity v from 500 to 2000 mm/s, and hatching space h from 50 to 120 μm. Note that building the sample at $P = 400$ W, $v = 1250$ mm/s, and $h = 90$ μm was interrupted because its rough top surface interfered with the powder recoater. Fig. 2(a–f, i) shows binarized optical microscopic images of the XY cross section of the samples in the first batch. In all samples, more defects were observed at the edges than inside the sample; Tang et al. observed a similar trend for the nickel superalloys CM247LC and IN939 [38]. In addition, Lam et al. [36] noted that cracking was likely to occur at the start, end, and turnaround points of the laser scanning strategies. Thus, for this study, the "inside" of the sample was defined as the 8 mm × 8 mm area just 1 mm inside the edge, as indicated by the yellow dashed square in Fig. 2.

The defects indicated by the black dots and lines in Fig. 2 were observed by SEM in detail. The linear defects in the optical microscope were cracks, as indicated by the red arrows in Fig. 3(a), and dendritic structures were observed in the fracture surface in the XZ plane indicated by the green arrow in Fig. 3(d). As reported in previous studies [17,31], such dendritic fracture surfaces were attributed to solidification cracking. Also, irregularly shaped pores (blue arrows in Fig. 3(b, e))

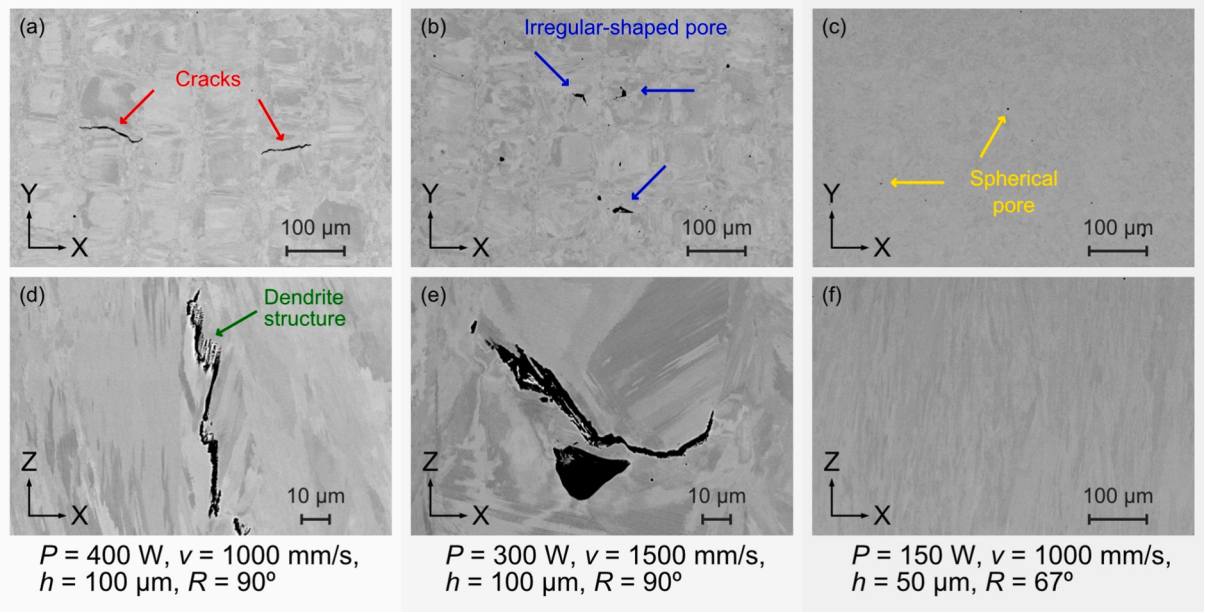

Fig. 3. SEM images of (a–c) XY and (d–f) XZ cross sections of the IN738LC samples at different laser power, scanning velocity, and hatching space.

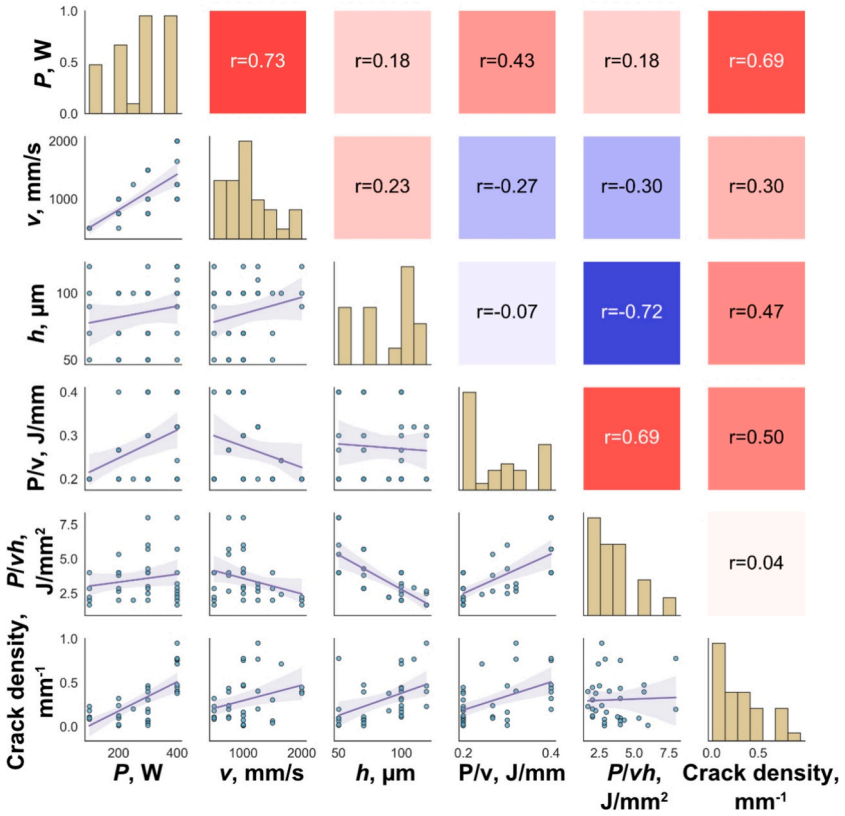

Fig. 4. Correlation matrix between laser scanning conditions and crack density for the sample built in the first batch. While the graphs on the lower left show scatter plots with a regression line and 95 % confidence interval, the numbers on the upper right indicate the correlation coefficient between each pair of the items.

were detected in some samples, and may have been caused by LOF [34,39]. In addition, minute spherical pores of smaller than 10 μm in diameter were present in all samples (see the yellow arrows in Fig. 3(c)), whereas spherical pores larger than 30 μm were observed in some samples, possibly due to keyholing [34,39].

Since there were such different types of defects in the samples, a crack in the optical microscope image in Fig. 2 was defined in this study as a defect with an aspect ratio >3.0. Each crack length was measured in the image analysis software, and the total length of all cracks was divided by the inside area (8 mm × 8 mm) to evaluate the crack density. The crack densities for each sample are described in Fig. 2 and Supplementary Table S1. Among the results shown in Fig. 2, the crack density was decreased with lowering P and narrowing h (see Fig. 2(a–c) and (b, f), respectively). On the other hand, the crack density was lower

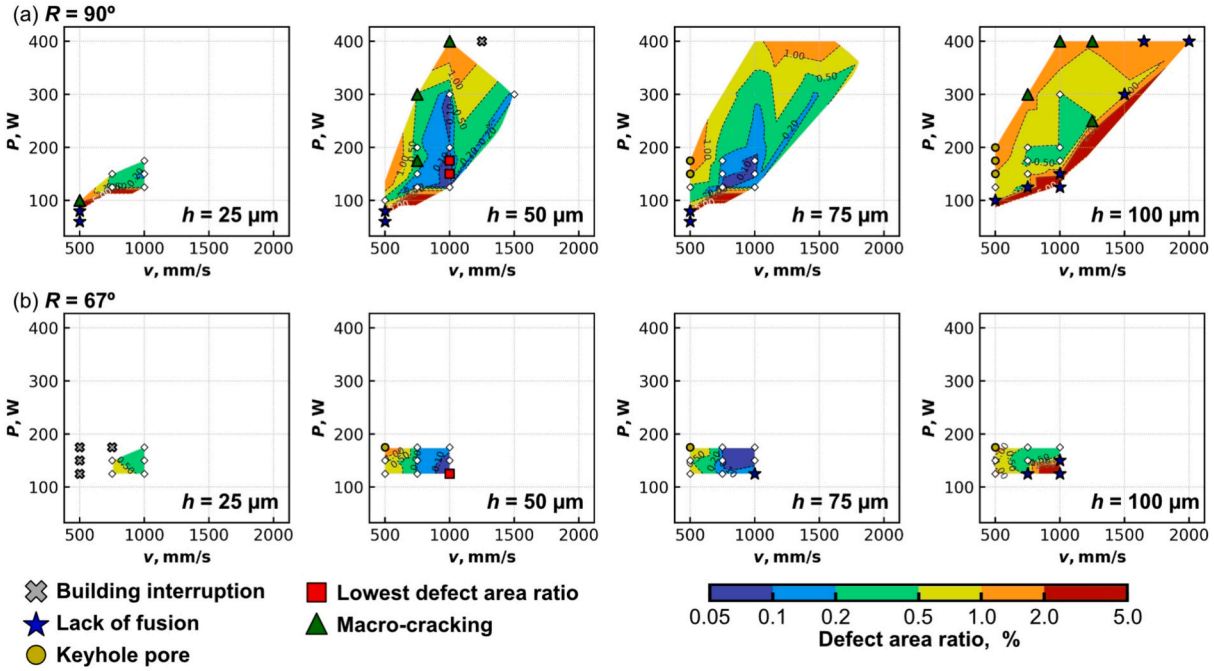

Fig. 5. Contour plots of the defect area ratio as a function of the laser scanning parameters. The rotation angle R is 90° for (a) and 67° for (b). Scatter plots indicate the laser scanning conditions actually tried in the experiment, with the gray crosses representing the conditions that caused building interruption. Among the scatter plots, irregularly shaped pores and relatively large spherical pores (>30 μm in diameter) were observed for the conditions represented by blue stars and yellow circles, respectively. The green triangles indicate the condition for the sample with macrocracking, and the red squares represent the conditions for the three samples with the lowest defect area ratios. (For interpretation of the references to color in this figure legend, the reader is referred to the web version of this article.)

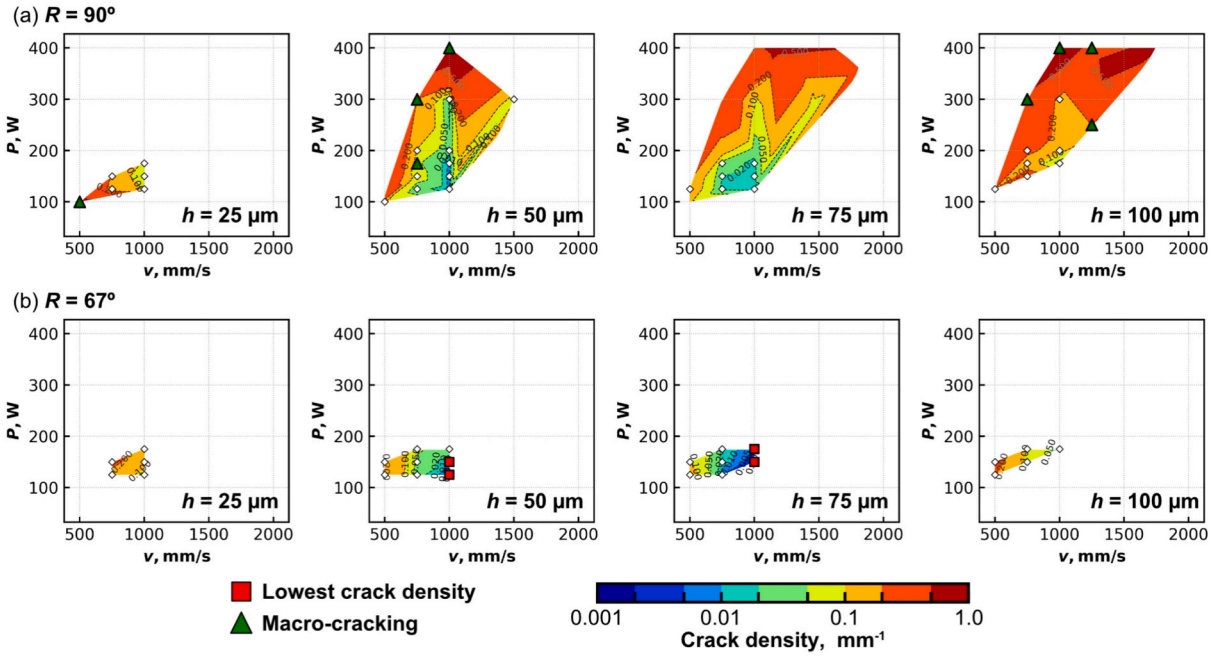

Fig. 6. Contour plops of crack density as a function of the laser scanning parameters. The rotation angle R is 90° for (a) and 67° for (b). Scatter plots indicate the laser scanning conditions actually tried in the experiment. The green triangles indicate the conditions for the sample with macrocracking, and the red squares represent the conditions for the four samples with the lowest crack densities. (For interpretation of the references to color in this figure legend, the reader is referred to the web version of this article.)

at a v of 1000 mm/s than at a v of 750 or 1500 mm/s (see Fig. 2(b, d, e)).

Fig. 4 shows the correlation matrix between the laser scanning parameters and crack density for all samples built in the first batch. Here, the laser energy densities P/v and P/vh were also added to the matrix. This matrix shows the histogram of each item on the diagonal, and the scatter plots and correlation coefficients for each combination of items in the lower left and lower right triangle areas, respectively. The tendencies in crack density with P and h described above are consistent with the scatter plots, and the correlation coefficients with crack density were highly positive, 0.69 for P and 0.47 for h. The lowest crack density of

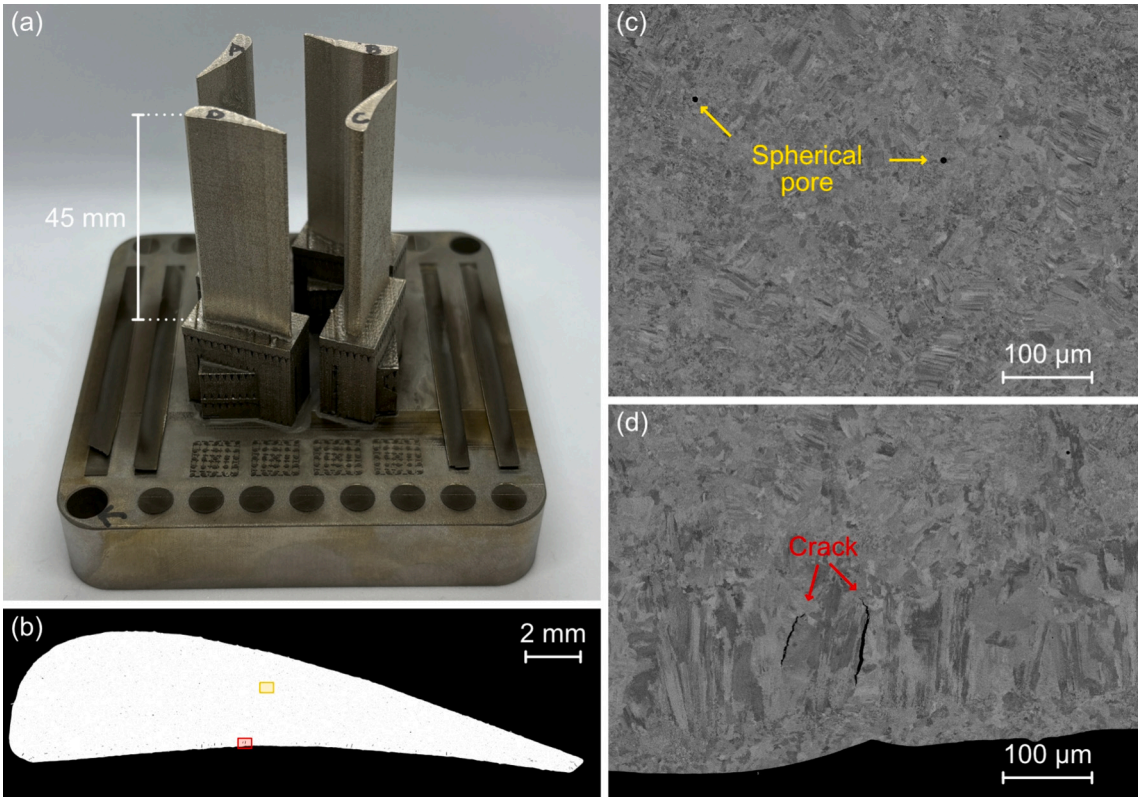

Fig. 7. (a) The as-built turbine blade-shaped parts, (b) a binarized optical microscopic image of the airfoil cross section. (c, d) SEM images for the central and edge regions in (b), respectively.

0.011 mm/mm^2 in the first batch was built with $P = 200$ W, $v = 1000$ mm/s, and $h = 70$ μm.

Based on these results of the first batch, the process map with P <200 W and h <100 μm was further explored in the second and third batches (see Fig. 1(c, d)). In addition, the rotation angle R was set to 67° for the second batch. For the conditions with $h = 25$ μm in the second and third batches, building of some samples was interrupted by interference with the recoater (the conditions are summarized in Supplementary Table S1), and the number of internal cracks is greater than for other samples fabricated with $h = 50$ μm. In addition, although there was a positive correlation between crack density and P in the first batch, the number of irregularly shaped pores increased when P was <100 W in the second and third batches. Consequently, among all the samples in the three batches, the laser scanning conditions that achieved a crack density below 0.005 mm/mm^2 were P and h of (125 W, 50 μm), (150 W, 50 μm), (150 W, 75 μm), and (175 W, 75 μm) with $v = 1000$ mm/s and $R = 67°$ (see sample IDs = 49, 61, 62, and 74 in S1). These samples with the lowest crack density had fewer defects at the sample edges, as shown in the outside of the yellow broken square in Fig. 2(g, h). Thus, as shown in Fig. 3(e, f), only minute spherical pores were observed in the sample.

The contour maps of the defect area ratio and crack density in Figs. 5 and 6, respectively, were created by integrating the results of the first to third batches. The defect area ratio was evaluated from the binarized optical microscope image, and the defects included cracks as well as spherical or irregularly shaped pores. In the contour map of the defect area ratio in Fig. 5, the plots with gray crosses represent the laser scanning conditions under which sample building was interrupted due to interference with the recoater. As indicated by the plots with blue stars in the contour map, LOF causing irregularly shaped pores occurred under conditions of lower P, faster v, or wider h. On the other hand, the plots with yellow circles represent spherical pores larger than 30 μm created by keyholing as observed by SEM when v was 500 mm/s and P was >150 W. The plots with green triangles in the contour map indicate conditions resulting in large cracks longer than 250 μm inside the sample (macrocracking). Fig. 2(i) shows a typical example of severe macrocracking caused by the crack propagation. As for the map of crack density in Fig. 6, the laser scanning conditions that resulted in less susceptibility to microcracking were lower linear energy density P/v and h in the range of 50 to 75 μm. Narrowing the h to 25 μm resulted in building interruption or macrocracking, and increased microcracking compared to the 50 μm cases. Consequently, it was found that the crack density and defect area ratio were <0.005 mm/mm^2 and 0.060 % under the conditions indicated by the plots with red squares in Figs. 5 and 6, respectively.

We then validated the above conditions as shown in Fig. 7(a). In brief, we fabricated turbine blade-shaped parts under the scanning condition of $P = 125$ W, $v = 1000$ mm/s, $h = 50$ μm, and $R = 67°$, since the condition was found to minimize the defect area ratio in the above analysis (i.e., they were one of the red squares in Figs. 5 and 6). The airfoil section was cut every 10 mm in height and the XY cross sections were observed by the microscopes. As an example, the optical microscope image and SEM images in the cross section at 40 mm height are shown in Fig. 7(b, c, d). Microcracks (Fig. 7(d)) were present only at the edge of the airfoil section and were seldom detected in the insides. On the other hand, the minute spherical pores shown in Fig. 7(b) were scattered throughout the cross section (Fig. 7(b)). Nevertheless, the defect ratio in all cross sections including the edges was still very low at 0.39±0.03 %. This result demonstrated that IN738LC parts with complex geometry and high density (low defect ratio) can be built using the optimal laser scanning condition.

3.2. Crystallographic orientation analysis

Fig. 8 shows the maps of the IPF-Z on the XY cross section observed by EBSD, where the respective laser scanning conditions are consistent with those in Fig. 2. In Fig. 8(a–e), where h is 100 μm, the

Fig. 8. Inverse pole figure (IPF-Z) maps of the XY cross section of samples fabricated under different laser scanning conditions as observed by EBSD.

microstructures were formed in a lattice pattern corresponding to the laser scanning strategy, and the square grains were surrounded by elongated grains oriented ⟨100⟩. In contrast, in the case of h of 50 μm, the grains are not lattice-like but irregularly shaped with serrated grain boundaries as shown in Fig. 8(f–h). It should be noted that such grains were formed not only when the rotation angle R was 67°, but also when it was 90° (see Fig. 8(f, h)). Such a transition from square to irregularly shaped grain morphology occurred at h around 70–75 μm, and irregularly shaped grains were definitely formed below 50 μm. In addition, when h was narrowed from 100 μm to 50 μm (see Fig. 8(b, f)), the crystal orientation was more oriented to around ⟨001⟩ over the cross section. When P was decreased to 150 W (Fig. 8(h)), the orientation was strongly aligned to ⟨001⟩ and the grain size became finer. From the EBSD results, the mean grain area and deviation angle of all the samples were evaluated and summarized in Supplementary Tables S2 and S3. Note that grain area represents the area-weighted average value, and the deviation angle refers to the mean angular difference between ⟨001⟩ and the Z-direction (building direction) and Y-direction. These evaluated values are in line with the qualitative tendencies described above. Fig. 9 shows the IPF maps in the XZ cross section, where the respective laser scanning conditions are consistent with those in Fig. 8(b, f–h). Basically, coarse grains that grew longer than 500 μm in the direction of fabrication are observed in Fig. 9, which is typical of nickel-based alloy materials fabricated in L-PBF [40,41].

Fig. 10 shows the maps of KAM and HAGBs for the EBSD results in the XY cross section in Fig. 8(b, f–h). As shown in Fig. 10(a), the KAM value was relatively high in the vicinity of the straight boundaries surrounding the square grains. In contrast, when h was narrowed to 50 μm (Fig. 10(b)), the KAM values inside the grains became as high as those near the grain boundaries, and the distribution was almost uniform over the cross section when P was further decreased to 150 W (Fig. 10(c)). In the case of $R = 67°$ (Fig. 9(d)), the KAM distribution was also uniform and similar to that of $R = 90°$. The mean KAM value is also added to Supplementary Tables S2 and S3.

In the HAGBs shown in Fig. 10(e–h), yellow straight lines indicate linear grain boundaries longer than 30 μm, as detected by the Hough transform. The linear grain boundaries were detected by loading the high grain boundary image obtained from the EBSD observation into Python and applying the probabilistic Hough transform with the OpenCV module [42]. In the case of $h = 100$ μm in Fig. 10(e), more than

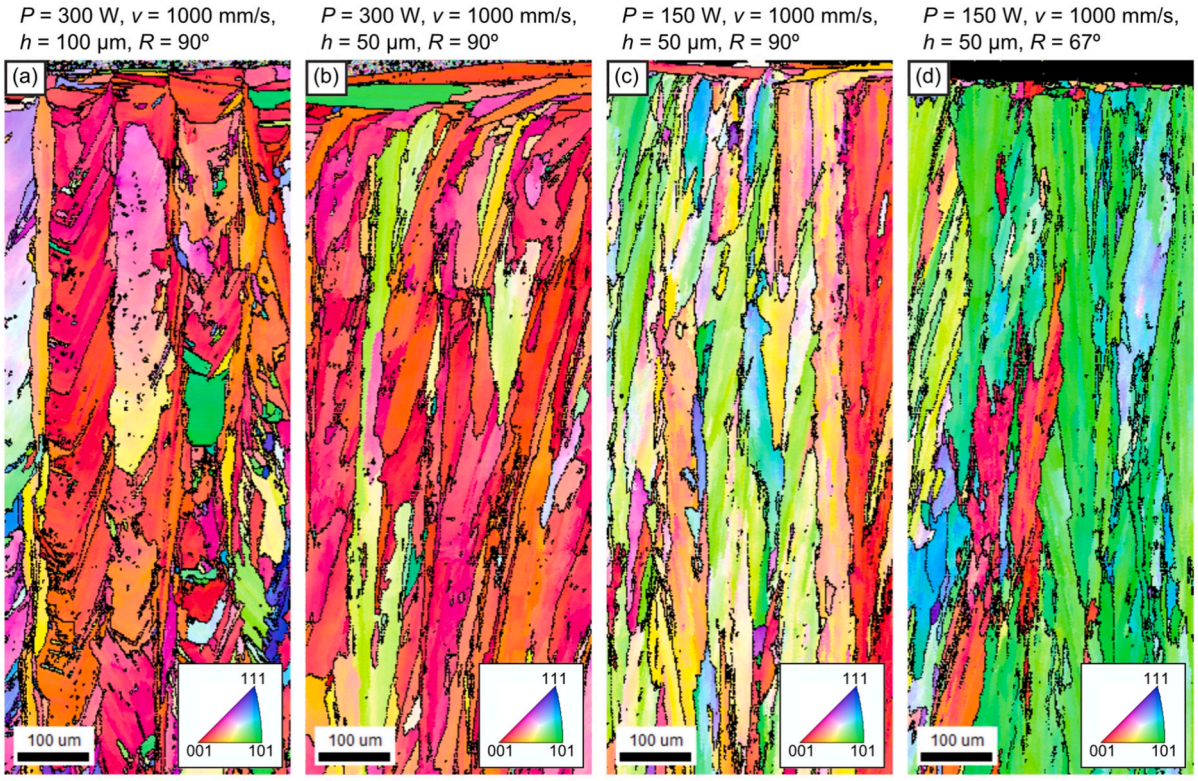

Fig. 9. Inverse pole figure (IPF-Y) maps of the XZ cross section of samples fabricated under different laser scanning conditions as observed by EBSD.

30 linear grain boundaries were detected within the 400 μm × 400 μm area. On the other hand, when *h* was narrowed to 50 μm, only a few linear grain boundaries were detected. The total length of linear grain boundaries per area was determined as the linear HAGB density and listed in Supplementary Tables S2 and S3. In addition, the fraction of HAGBs is defined as the ratio of grain boundary lengths with misorientation >15° to the total grain boundary length, as in Chen et al. [18]. The fraction of HAGBs also follows a similar trend as the grain area and

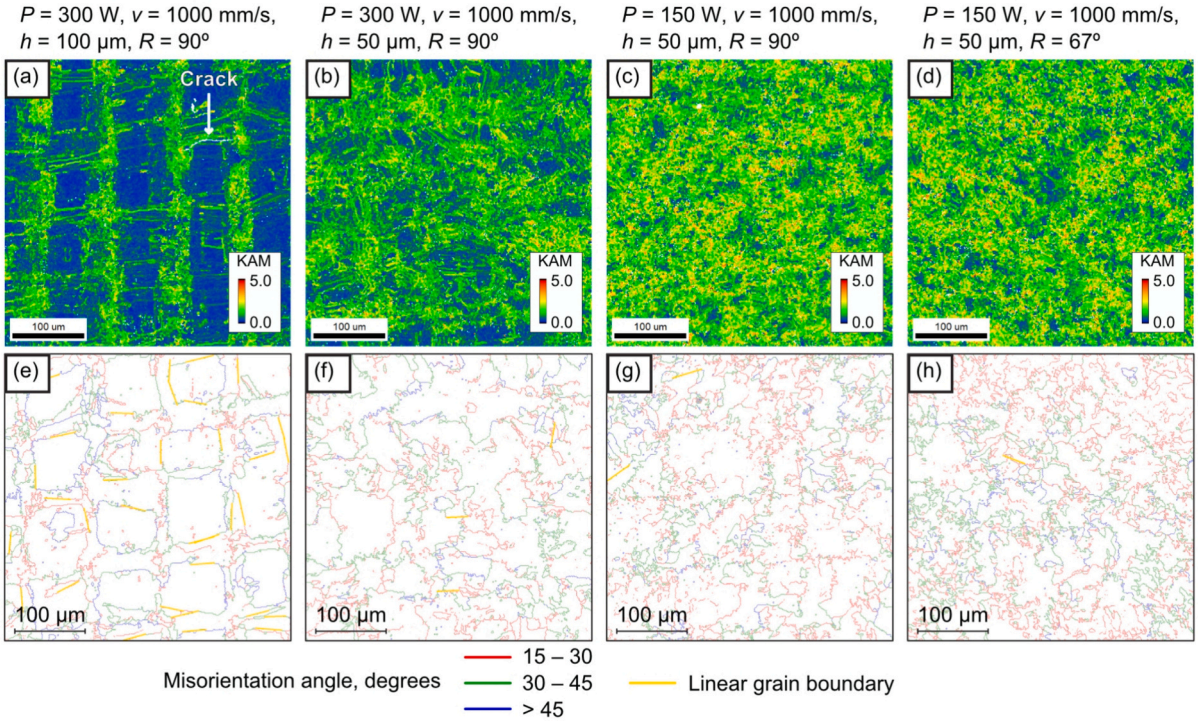

Fig. 10. (a–d) Kernel average misorientation (KAM) and (e–h) high angle grain boundary (HAGB) map of the XY cross section of samples fabricated under different laser scanning conditions as observed by EBSD. The yellow line in (e–h) represents the straight HAGB grain boundary detected by Hough transform. (For interpretation of the references to color in this figure legend, the reader is referred to the web version of this article.)

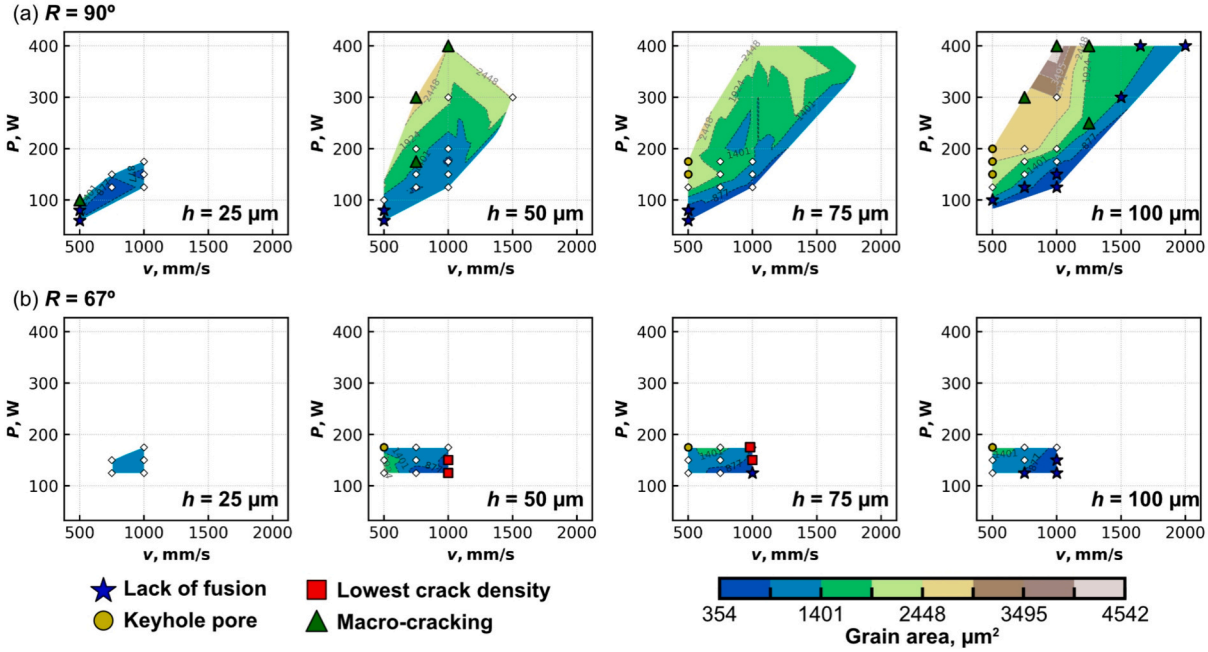

Fig. 11. Contour plots of grain area in the XY cross section observed by EBSD as a function of laser scanning parameters. The rotation angle R is 90° for (a) and 67° for (b). Scatter plots indicate the laser scanning conditions actually tried in the experiment. Among the scatter plots, irregularly shaped pores and relatively large spherical pores (>30 μm in diameter) were observed for the conditions represented by the blue stars and yellow circles, respectively. The green triangles indicate the conditions for the sample with macrocracking, and the red squares represent the conditions for the four samples with the lowest crack densities. (For interpretation of the references to color in this figure legend, the reader is referred to the web version of this article.)

linear HAGB density—i.e., it decreases with narrower h and lower P.

Figs. 11 to 13 show contour maps of grain area, linear HAGB density, and deviation angle to Z-direction based on the EBSD observations at the XY section for all the fabricated samples. As seen in the lower right area of the contour map in Fig. 11, the crystal grain became finer as P/v decreased. In addition, the contour maps indicate that all three of these microstructural features became smaller as h narrowed. However, the grain area and the deviation angle increased when h was narrowed to 25 μm. For example, Fig. 14 shows the optical microscope image and IPF maps for the sample fabricated with the laser scanning parameters of

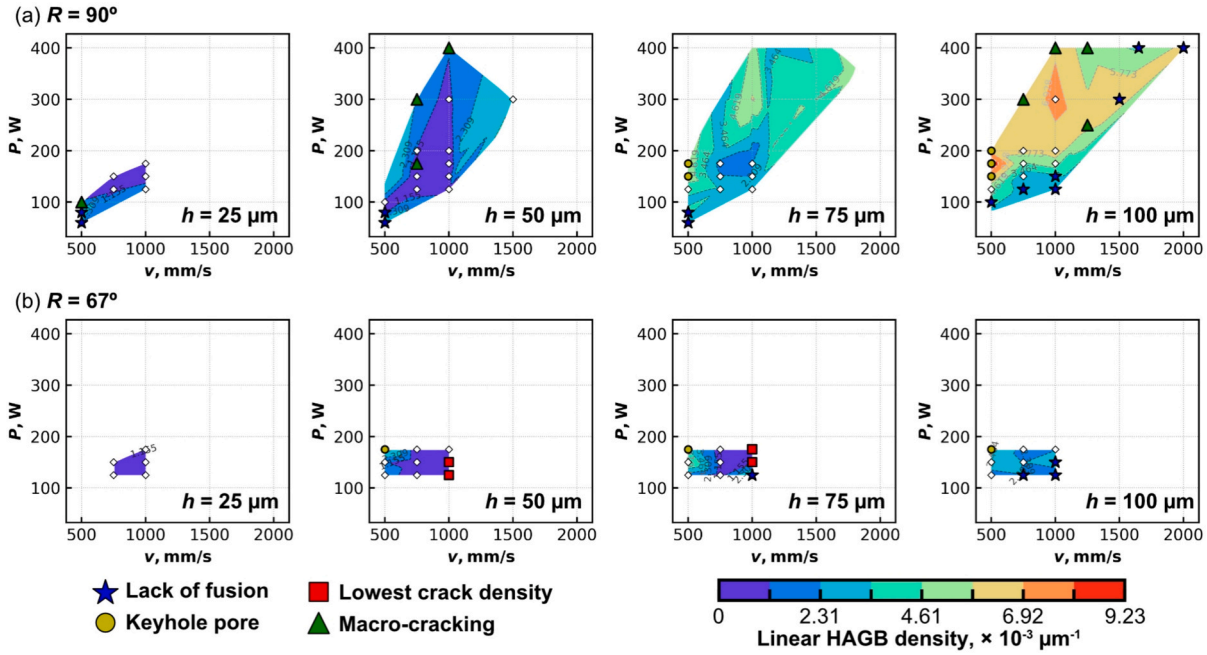

Fig. 12. Contour plots of linear HAGB density in the XY cross section observed by EBSD as a function of laser scanning parameters. The rotation angle R is 90° for (a) and 67° for (b). Scatter plots indicate the laser scanning conditions actually tried in the experiment. Among the scatter plots, irregularly shaped pores and relatively large spherical pores (>30 μm in diameter) were observed for the conditions represented by the blue stars and yellow circles, respectively. The green triangles indicate the conditions for the sample with macrocracking, and the red squares represent the conditions for the four samples with the lowest crack densities. (For interpretation of the references to color in this figure legend, the reader is referred to the web version of this article.)

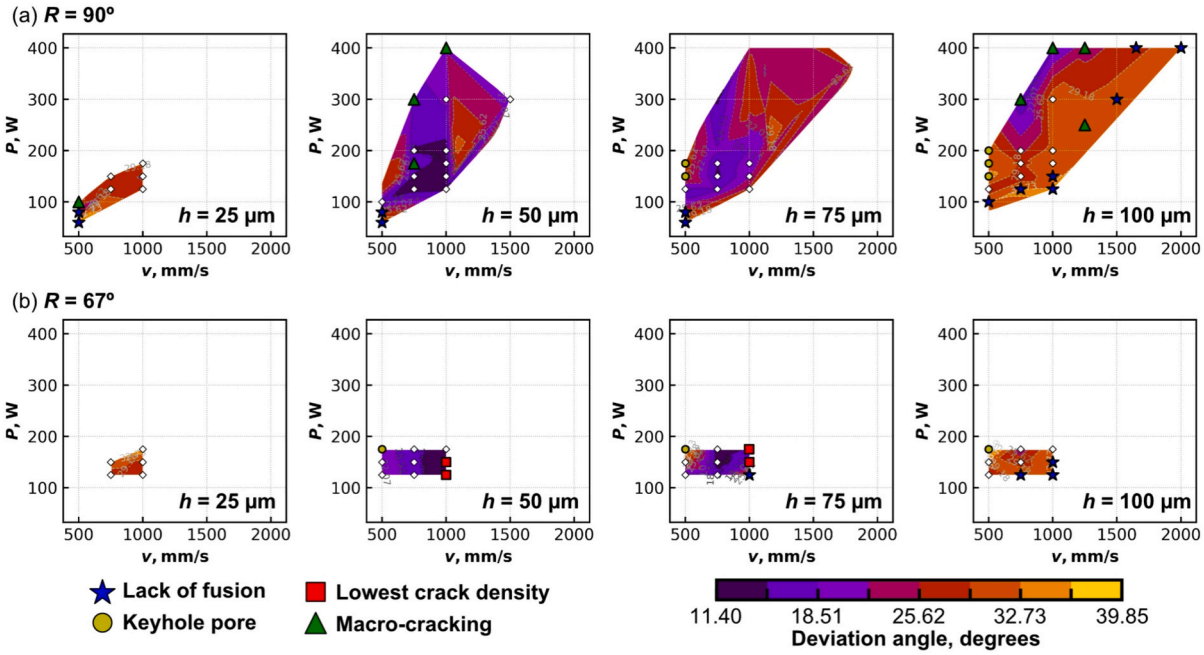

Fig. 13. Contour plots of deviation angle in the XY cross section observed by EBSD as a function of laser scanning parameters. The rotation angle R is 90° for (a) and 67° for (b). Scatter plots indicate the laser scanning conditions actually tried in the experiment. Among the scatter plots, irregularly shaped pores and relatively large spherical pores (>30 μm in diameter) were observed for the conditions represented by the blue stars and yellow circles, respectively. The green triangles indicate the conditions for the sample with macrocracking, and the red squares represent the conditions for the four samples with the lowest crack densities. (For interpretation of the references to color in this figure legend, the reader is referred to the web version of this article.)

$P = 150$ W, $v = 1000$ mm/s, $h = 25\,\mu$m, and $R = 67°$. Although this condition differs from the one with $h = 50\,\mu$m, which resulted in a crack density of <0.005 mm/mm^2 (see Fig. 2(g)), the crack density increased to 0.122 mm/mm^2, as shown in Fig. 14(a). The microstructure of this sample consists of irregularly shaped grains with serrated HAGBs, similar to the case with $h = 50\,\mu$m (see Fig. 14(b, c), Fig. 8(g), and Fig. 9 (d)). However, in the case of 25 μm as shown in Fig. 14(b), these grains exhibit a variety of orientations including ⟨101⟩ with respect to the Z direction. The mean grain area and the deviation angle in the Z direction in were 1203 μm^2 and 791 μm^2, and 27.5° and 11.4° for the 25 μm and 50 μm hatching space, respectively (see also Supplementary Tables S2 and S3). It is also noteworthy that, on the XZ plane in Fig. 14(c), the columnar grains appear to grow at an angle with respect to the Z-axis.

3.3. Causal analysis between laser scanning, microstructures, and microcracking

In the previous sections, microcracking and microstructures were observed for each sample under different laser scanning conditions, and the evaluated values were stored in the datasets presented in Supplementary Tables S2 and S3. In order to examine the linear relationship among laser scanning parameters, microstructural features in the XY and XZ section, and crack density, correlation matrices were created as shown in Figs. 15 and 16, respectively. As a pre-processing step, samples with large spherical pores created by keyholing, irregularly shaped pores by LOF, or macrocracks (the plots with yellow circles, blue stars, and green triangles in Fig. 5) were removed from the dataset.

By referring to the rightmost column of these matrices, it can be seen that the grain area and linear HAGB density in the XY section, KAM, and deviation angle in the Z direction in both sections were correlated with crack density. Since a high absolute correlation coefficient does not necessarily imply a causal relationship of the microstructural feature to microcracking, the direction of causality should be carefully considered. For example, there is a negative correlation between KAM and crack density (−0.48 and −0.40 in the XY and XZ direction). As shown in Fig. 10(a–d), the KAM value within the grain increased to the same level as that near the grain boundaries, increasing the average KAM values. Strain in the grains may have accumulated as a result of suppressing microcracking at the grain boundaries, which would have prevented tensile stresses from being released. This is similar to the higher residual stresses observed in as-fabricated IN738LC samples with lower crack densities, resulting from less stress relaxation, as reported by Hafezi et al. [34].

The correlation coefficient between grain area in the XY section and crack density was 0.53, suggesting the inhabitation of microcracking by grain refinement. Consistent with the trend in the contour map in Fig. 11, the correlation coefficients of grain area with h and P/v were 0.42 and 0.63, respectively. On the other hand, the correlation coefficient for grain area in the XZ section was <0.4 with crack density or with any of the laser scanning parameters. Actually, the microstructures in the XZ section in Fig. 9 show similar columnar grains along the building direction and no clear difference in grain area even among samples with different crack densities and scanning conditions.

Such grain refinement was also closely related to the morphology of HAGBs, so that the grain size in the XY section was correlated with both the fraction of HAGB and linear HAGB density (0.48 and 0.68, respectively), whereas their coefficients in the XZ section were <0.4. The correlation coefficients between the fraction of HAGBs and crack density were low (0.27 and 0.28 in the XY and XZ sections), and the scatterplots in Figs. 15 and 16 show that the crack density was not minimal at the minimum value of the fraction. While the fraction of HAGBs was highly and positively correlated with h, the crack density tended to increase when h was narrowed to 25 μm. Compared with the fraction of HAGBs, linear HAGB density had slightly higher correlation coefficients with crack density (0.44 and 0.37 in the XY and XZ sections, respectively), which could explain the effect of serrated grain boundaries on crack inhibition. In addition to the relatively high positive correlation with h seen in the contour plots in Fig. 12, linear HAGB density in the XY section was also somewhat correlated with P and P/v. In the XZ section, however, linear HAGB density was only correlated with h in the laser

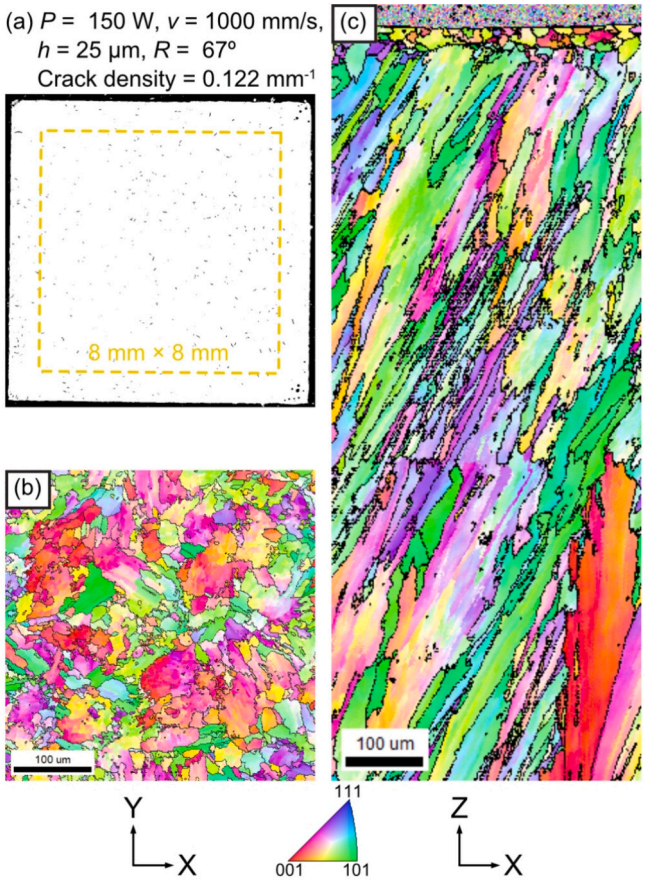

Fig. 14. (a) Binarized optical microscope image of the XY cross section, (b) inverse pole figure (IPF-Z) map of the XY cross section, and (c) inverse pole figure (IPF-Y) map of the XZ cross section for the sample fabricated with laser scanning parameters of $P = 150$ W, $v = 1000$ mm/s, $h = 25$ μm, and $R = 67°$. The yellow dashed rectangle of 8 mm × 8 mm indicates the inside bound of the sample. (For interpretation of the references to color in this figure legend, the reader is referred to the web version of this article.)

scanning parameters.

With respect to the deviation angle, first, this angle should be similar in any section by its definition, and in fact, the deviation angles in the same direction at the XY and XZ sections were highly correlated (0.85 and 0.86 in the Z and Y directions, respectively). Thus, the trend in the deviation angles in the XY section are described here as a representative result. The correlation coefficient between the deviation angle in the Z direction and crack density was 0.59, which was the highest correlation with crack density among the microstructural features. As for the deviation angle in the Y direction, there was no correlation with the crack density. Since ⟨001⟩ is the preferential growth direction of FCC metals, the small deviation angle indicates that the ⟨001⟩ of neighboring grains grew together in the Z direction during solidification, which may have decreased the susceptibility to solidification cracking. As shown in Fig. 15, the deviation angle in the Z direction had low correlation coefficients with all of the process parameters, but it appeared to increase with increasing h, except when h was 25 μm. Thus, h is considered to be an important parameter that affects the texture aligned in the building direction.

Then, to evaluate the contribution of several microstructural features together to microcracking, a prediction model for crack density was constructed using multiple linear regression (MLR), support vector regression (SVR), and random forest regression (RFR) based on the microstructural features in the dataset. These regression models were implemented in Python (version 3.12.10) using the scikit-learn package (version 1.6.1) [43]. Here, the KAM values were excluded from the dataset because the causal contribution of KAM to microcracking cannot be explained, as described above. MLR models were built for all combinations of microstructural features, and the best combination was screened based on a mean squared error (MSE) between the measured and predicted crack density (feature selection). The values in the dataset were standardized in the preprocessing, and leave-one-out cross validation (LOOCV) was performed to avoid over-training of the prediction model. For more details on MLR, feature selection, and LOOCV, refer to our previous paper for the prediction of tensile properties from microstructural features of titanium alloys [44].

The heat map in Fig. 17(a) shows the 10 combinations with the lowest MSE among all combinations of microstructural features, and the color and value indicate the coefficient of the MLR model. Basically, the grain size in the XY section and the deviation angles in the Z direction were essentially selected in any combination with the small MSE. While some models included the deviation angle in the Y direction, and the fraction and linear density of HAGBs were barely chosen for the top 10 models. The equation used to predict crack density by the combination of microstructural features that minimize MSE was as follows:

$$CD = 5.01 \times 10^{-5} GA_{XY} + 6.50 \times 10^{-3} DA^{Z}_{XZ} - 1.21 \times 10^{-1} \quad (1)$$

where CD, GA, and DA represent crack density, grain area, and deviation angle, respectively. While the subscript of variables indicates the cross section, the superscript represents the direction of the deviation angle. In addition, the units of GA and DA are μm^2 and degrees before standardization. As shown in Fig. 17(b), the scatter plots of the predicted crack density against the measured one tend to follow a solid diagonal line, but there is a lot of variation. The mean absolute error (MAE), the correlation coefficient R, and the coefficient of determination R^2 were 0.0456 mm/mm^2, 0.665, and 0.442 respectively (see Table 2).

Similarly, nonlinear regression models, SVR and RFR, were also constructed to predict crack density prediction using the same dataset. A 5-fold cross validation was performed for each model to avoid overfitting. The hyperparameters for each model were optimized to maximize the R^2 score using a grid search, and the results are summarized in Table 3. Then, the SVR and RFR models with the best hyperparameters were used to predict the crack density, and the results were plotted against the measured values in Fig. 17(d, f). The corresponding prediction scores were added to Table 2. These results indicate that the prediction performance of these nonlinear models was not particularly high and was comparable to that of the MLR model in Fig. 17(b). In particular, when the crack density exceeds 0.2 mm/mm^2, all regression models tend to underestimate the values, suggesting that some critical features relevant to more severe solidification cracking may be missing in the dataset. In these nonlinear regression models, permutation importance was evaluated as a relative measure of how each parameter contributes to the prediction. As shown in Fig. 17(c, e), the importance of the ⟨001⟩ deviation angle to Z-direction was relatively high in both models.

Univariate sensitivity analysis using the one-at-a-time (OAT) method was conducted for GA_{XY} and DA^{Z}_{XZ} screened by the feature selection in the MLR model (Fig. 17(a)). The target variable was varied from its minimum to maximum value in the dataset, while all other variables were fixed at their mean values, and the crack density was predicted to evaluate the contribution of the target variable. As plotted in blue in Fig. 17(g, h), both variables GA_{XY} and DA^{Z}_{XZ} positively contributed to the increase in crack density in the MLR model, and their influence on the prediction was similar. The confidence intervals shown in gray were wider at both ends of the variable due to the relatively limited number of data points. Although SVR is a nonlinear model, the plot in red showed a similar trend to that of MLR. In contrast, the RFR model (see green plot in the figure) showed that crack density was almost insensitive to GA_{XY}, while DA^{Z}_{XZ} contributed to the crack density in non-continuous increments. This trend and the low predictive performance of the RFR model are likely due to the prioritization of generalization performance

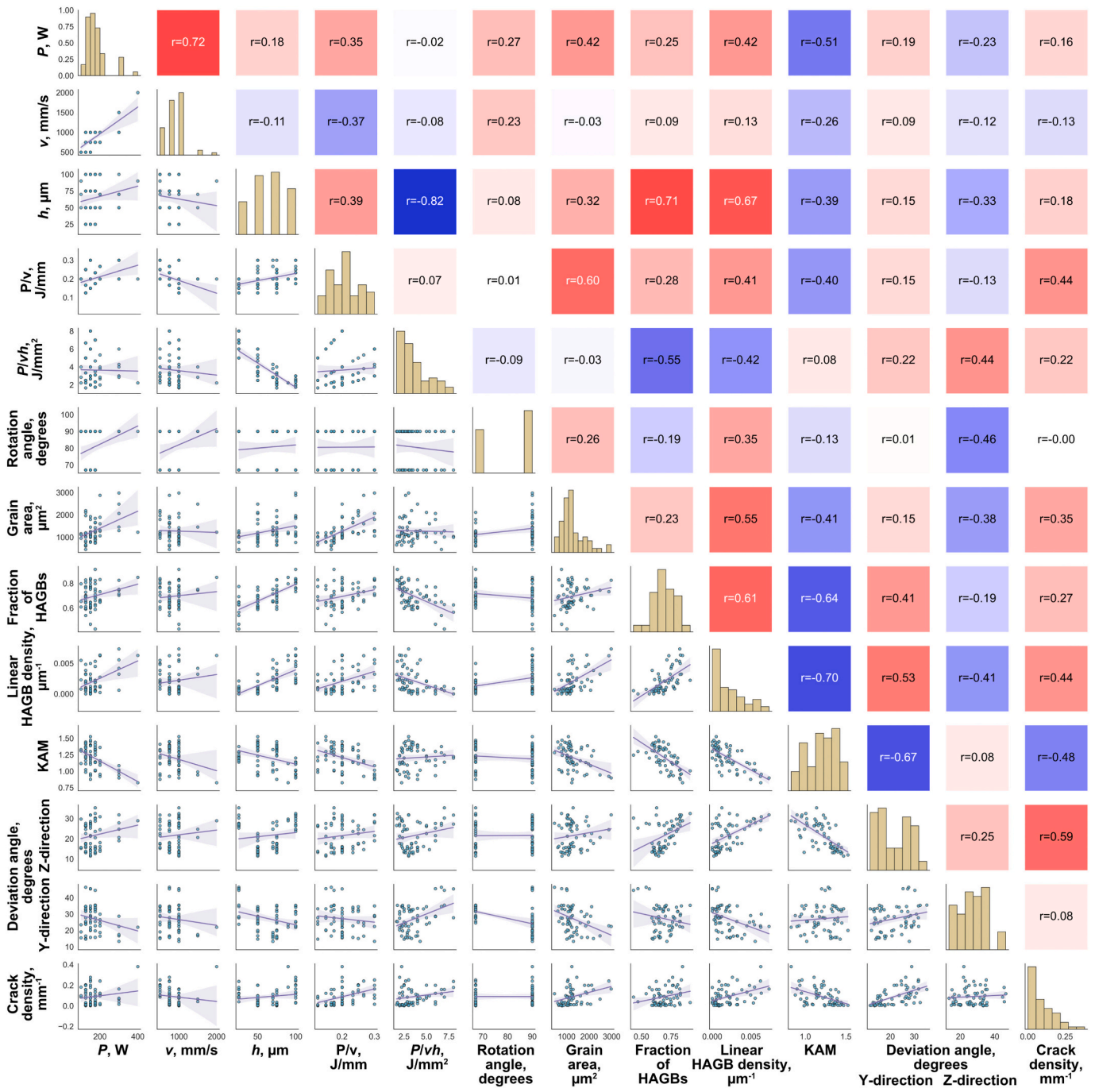

Fig. 15. Correlation matrix of the laser scanning parameters, microstructural features at the XY section, and crack density.

in cross-validation, despite the limited size of dataset.

In the same way, GA_{XY} and DA^{Z}_{XZ} were also predicted form the laser scanning parameters using the respective equations:

$$GA_{XY} = 6350P/v + 11.8R - 953 \quad (2)$$

$$DA^{Z}_{XZ} = -0.173P + 375 \times 10^{-2}v + 0.649h + 9.18P/vh - 55.8 \quad (3)$$

As shown in the scatter plots of the predicted and measured values in Fig. 18, GA_{XY} and DA^{Z}_{XZ} appeared to be aligned with the diagonal solid line. The prediction scores of MAE, R, and R^2 were 17.5 μm^2, 0.658, and 0.433 for GA_{XY}, and 3.30°, 0.822, and 0.677 for DA^{Z}_{XZ}, respectively.

4. Discussion

As described in Section 3.1, the optimal laser scanning conditions to minimize the defect in the rectangular IN738LC sample were empirically found, and were also validated by application to the fabrication of turbine blade-shaped parts. Thus, the optimal conditions would be also effective to build parts with more complex geometries and real-scale components with fewer defects. In addition, the successful suppression of solidification cracking in IN738LC, which is more susceptible than IN718 and IN625 [9], suggests that optimal building conditions for crack-free parts can be effectively identified through this data-driven approach, even for more challenging superalloys such as IN939 and CM247LC. In such cases, due to the similar thermal properties and the common preferential grain growth direction, the optimal laser scanning

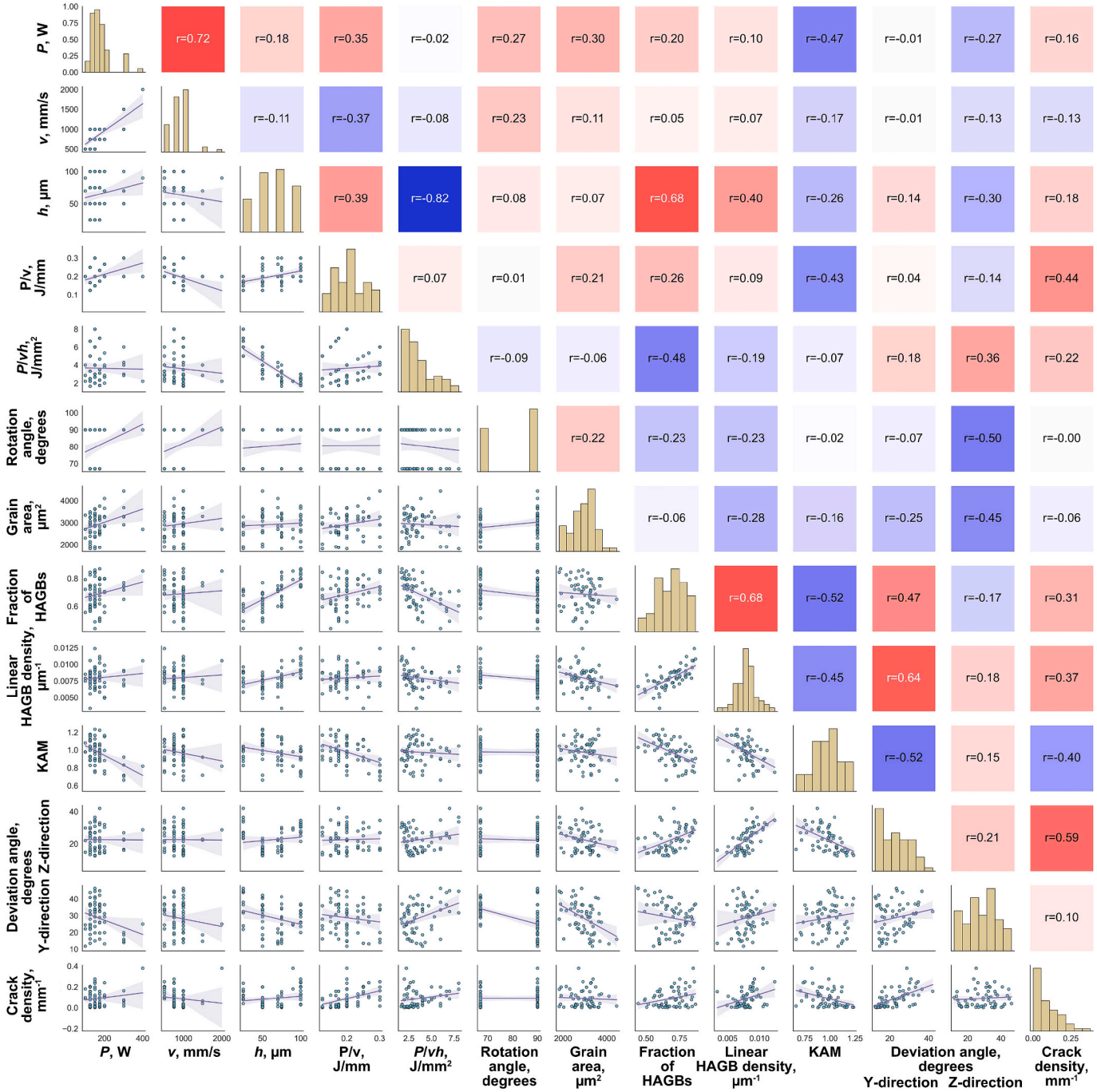

Fig. 16. Correlation matrix of the laser scanning parameters, microstructural features at the XZ section, and crack density.

conditions found for IN738LC can be adapted with minor tuning for other nickel-based superalloys. At the same time, it is important to consider the influence of minor alloying element segregation and secondary phase precipitation on solidification cracking when applying this approach to other high-temperature alloys or different material systems.

On the other hand, the process window with few defects for IN738LC is limited, which constrains the further adjustment of the laser scanning parameters to control microstructures (for site-specific and functionally degraded properties, for example). To further expand the process window, it may be worth exploring areas where the scanning velocity is increased from 1000 mm/s (see the red squares in Fig. 6) until the irregularly shaped pores are confirmed due to LOF. Actually, the laser scanning conditions for crack-free IN738LC samples in the referenced studies were higher power and faster scanning velocity than those used in the current study (P =210 W and v = 1750 mm/s for Chen et al. [41] and P = 250 W and v = 1300 mm/s for Hafezi et al. [34]). The rotation angle of 67° in the meander strategy was the most crack-suppressive in both the current study and the previous ones [12,34,36,41], but there may still be room for further investigation of scanning strategies that are more complex, such as fractal patterns [45]. Such scanning strategies may also suppress the cracks at edges observed in Fig. 2, which may have been caused by the irregular thermal history at turnaround points [36]. In addition, although not used in the present study, the preheating function in the L-PBF machine may expand the process window with fewer cracks as in the previous study [18].

In Section 3.3, the prediction model of crack density from microstructural features suggested that grain refinement and alignment of ⟨001⟩ to the Z direction suppressed microcracking. A similar trend was

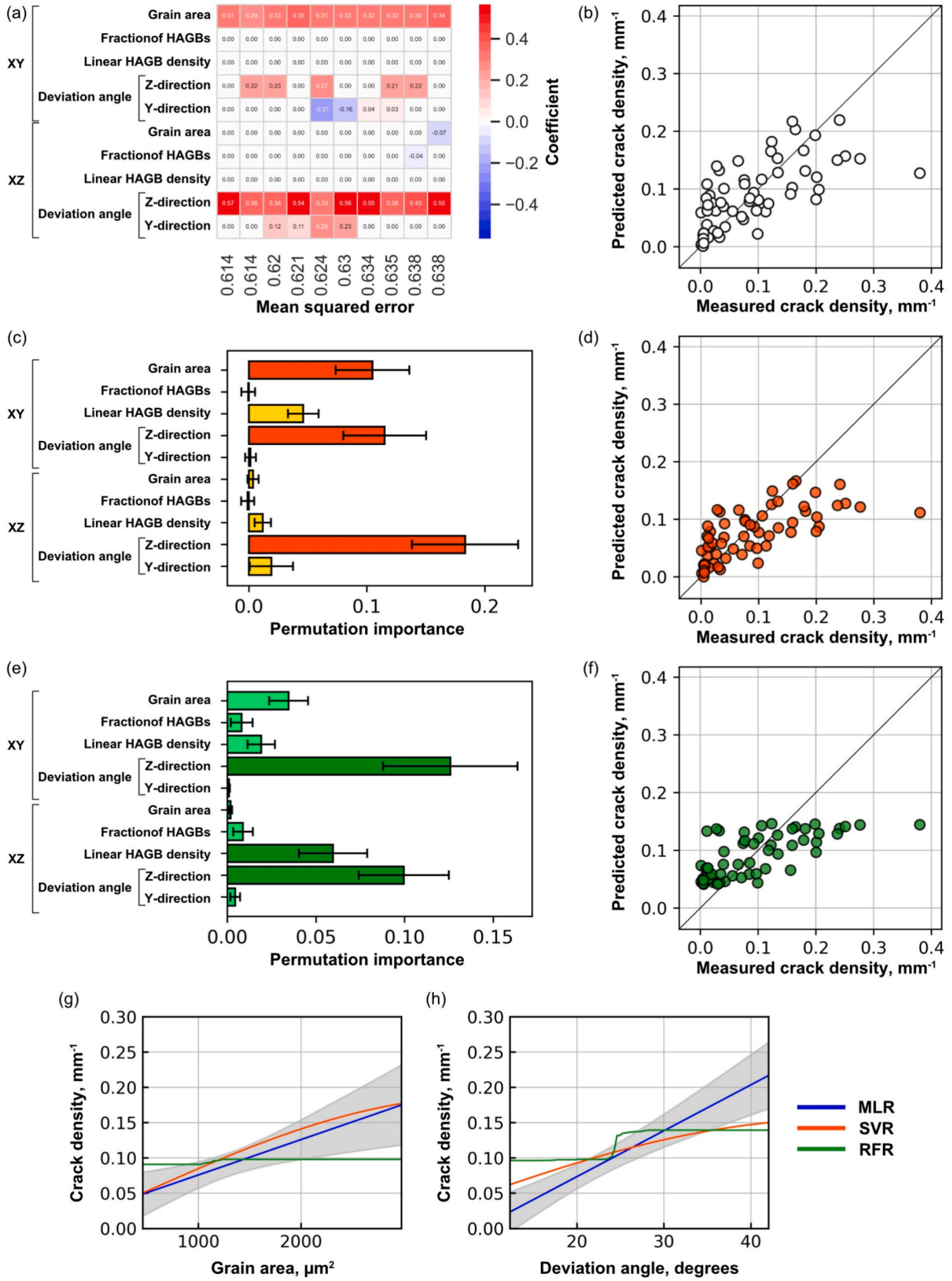

Fig. 17. (a) Heat map of 10 combinations of microstructural features up to the 10th mean squared error in ascending order for predicting crack density, as identified by LOOCV, (b) and scatter plot of the predicted crack density against the measured one using the MLR model. (c, e) Permutation importance of each microstructural feature, and (d, f) scatter plot of the predicted versus measured crack density using the SVR and RFR models, respectively. Results of univariate sensitivity analysis for (g) grain area GA_{XY} and (h) deviation angle DA^{Z}_{XZ}. The error bars in (c) and (e) represent the standard deviation of the permutation importance.

Table 2
Mean absolute error (MAE), the correlation coefficient R, and the coefficient of determination R^2 for multiple linear regression (MLR), support vector regression (SVR), and random forest regression (RFR).

Model	MAE, mm/mm^2	R	R^2
MLR	0.0456	0.665	0.442
SVR	0.0439	0.643	0.413
RFR	0.0502	0.648	0.420

Table 3
Best hyperparameters for support vector regression (SVR) and random forest regression (RFR).

Model	Hyperparameters	Value
SVR	Regularization parameter	0.1
	Negligible margin of error	0.01
	Scale of RBF kernel	0.01
RFR	Minimum number of samples in a leaf	12
	Number of estimators	200

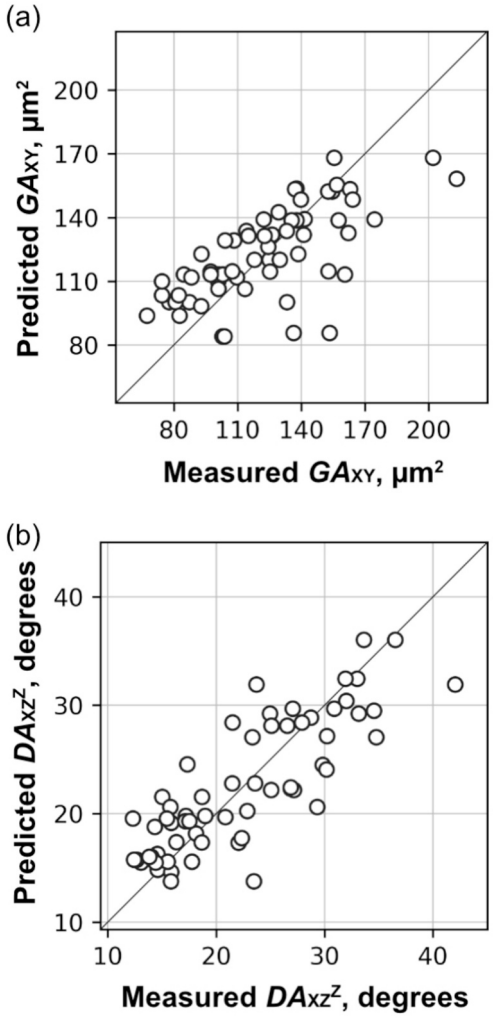

Fig. 18. Comparison of predicted and measured values for (a) GS_{XY} and (b) DA^{Z}_{XZ}.

observed when the hatching space was further narrowed form 50 μm to 25 μm. In the field of welding [6], coarse columnar grains promote solidification cracking due to strain concentration along the grain boundaries, whereas fine equiaxed grains reduce crack susceptibility by dispersing strain and enhancing liquid permeability. As demonstrated in the theoretical study by Kou [46], grain refinement mitigates solidification cracking not only by distributing transverse tensile strain across more grain boundaries, but also by promoting grain coalescence through the increased surface area per unit volume, which disrupts the continuity of intergranular liquid film. Also, it is reasonable that the crack density decreased in samples with fine grains since grain boundaries serve to stop crack propagation. As shown in Fig. 3(a), once formed, the cracks propagated along the grain boundaries until they reached the fine grains. From the perspective of crack propagation, it is worth noting that, as shown in the correlation matrix in Fig. 15, the fraction of HAGBs in the XY plane is 0.27, whereas the linear HAGB density is slightly higher at 0.44. This result suggests that cracks do not simply propagate along HAGBs, but rather tend to follow more linear grain boundaries than serrated ones. This observation is consistent with a previous study [21], which reported that not only grain refinement but also the formation of serrated grain boundaries contributed to the suppression of microcracking in L-PBF samples fabricated from IN738LC raw powders mixed with TiC nanoparticles.

Since the preferential growth direction of FCC metals is ⟨001⟩, alignment of ⟨001⟩ to the Z direction indicates that the crystal grains grew with ⟨001⟩ in the Z direction during solidification. This is consistent with the phase-field study [12] indicating that an increase in misorientation angle results in higher grain boundary energy and larger dendrite spacing, both of which contribute to crack susceptibility. Indeed, for example, in the case of a hatching space of 25 μm, a variety of orientations including ⟨101⟩ with respect to the Z direction were observed, as shown in Fig. 17(b). As a result, the crack density increased to 0.122 mm/mm^2, compared to 0.004 mm/mm^2 in the case of 50 μm. Moreover, the dendrite spacing increases in convergent rather than divergent grain boundaries [10,11]. Such dendrite spacing could act as initiation sites for solidification cracking. Fig. 19 shows SEM images of the cross section with the cellular dendrites clarified by electro-etching (12 ml H_3PO_4, 40 ml HNO_3, and 48 ml H_2SO_4 [47]). As indicated by the black arrows in Fig. 19(b), the cellular structures appear to diverge at the grain boundary due to difference in the preferential growth orientation of ⟨001⟩. The cavity between the structures, as marked by the white arrow in Fig. 19(b), likely formed due to insufficient liquid feeding during solidification, leading to the nucleation of the crack.

Although grain refinement and the alignment of ⟨001⟩ to the Z direction are essential for explaining the mechanism of solidification cracking, the poor predictive performance of the regression models, as shown in Fig. 17 and Table 3, suggests that the dataset still lacks fundamental characteristics. In the previous studies, microsegregation of minor impurities [13–17] and secondary phase precipitates [13,14,18–20] have been observed on the crack fracture surface. To incorporate such fine-scale phenomena into the prediction model, more detailed observations using an electron probe micro analysis (EPMA), X-ray diffraction (XRD), transmission electron microscopy (TEM), and atom probe tomography (APT) are required, along with dedicated efforts to extract relevant quantitative features. Such segregation and precipitation are also influenced by the cyclic thermal history caused by the repeated laser scanning in L-PBF, both track by track and layer by layer. Therefore, the temperature fields obtained through multiscale thermal analysis and temperature field monitoring would be helpful in considering their contribution to solidification cracking.

As for the mechanical factors that tensile strain applied to liquid film (see the yellow arrows in Fig. 19(b)), the evaluation of incremental plastic strain and critical strain rate in single bead-on-plate test is undoubtedly useful for elucidating the relationship between laser scanning conditions and solidification cracking as highlighted in the previous studies [25,26] referred in the Introduction, and it has the potential to improve the accuracy of our prediction model. On the other hand, applying the thermal elastoplastic analysis to actual sample fabrication processes involving multi-track laser scanning and layer-by-layer builds results in an exponential computational cost. Thus, developing efficient

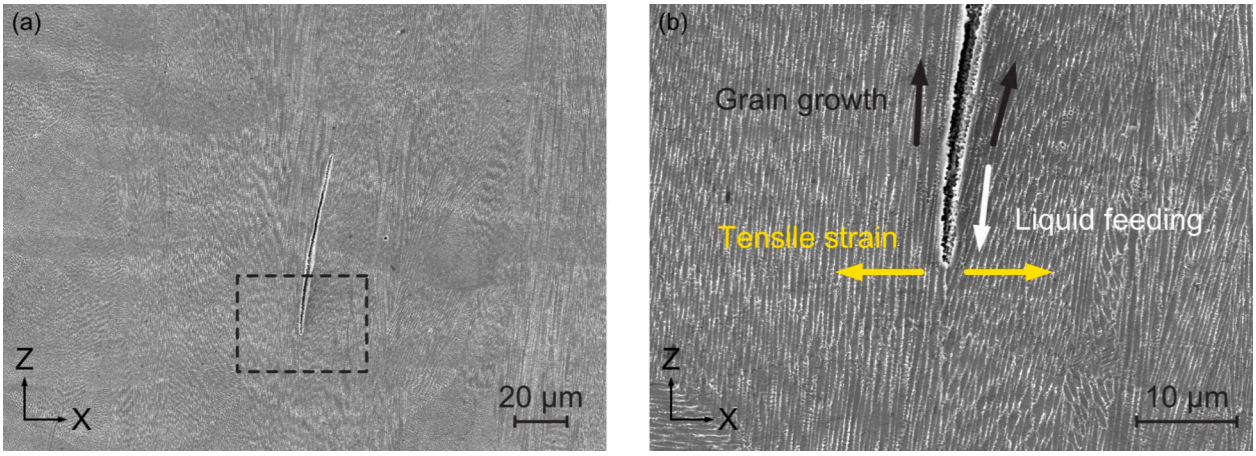

Fig. 19. SEM images of the electro-etched cross section of the sample fabricated with the laser scanning conditions of $P = 100$ W, $v = 500$ mm/s, $h = 100$ μm, and $R = 90°$. (b) shows an enlarged view of the region outlined by the black broken rectangle in (a), including the crack tip between the cellular dendrites.

techniques to address this challenge will be a critical focus of future research.

5. Conclusion

In this study, the laser scanning conditions were experimentally explored for building defect-free nickel-based superalloy IN738LC components in L-PBF. By fabricating rectangular samples under significantly different conditions, not only microcracks but also irregularly shaped pores, spherical pores, and macrocracks were found within the samples. These defects were classified and measured in order to develop the process maps of defect rate and crack density. Among more than 100 conditions, the optimal laser scanning conditions were found to minimize the defect ratio and crack density to <0.060 % and 0.005 mm/mm^2, respectively. Turbine blade-shaped parts without internal defects were successfully built using the optimal conditions. Crystal orientation analysis of the as-fabricated samples and subsequent causal analysis with multiple linear regression revealed that primarily the grain refinement and the alignment of ⟨001⟩ to the building direction during solidification suppressed microcracking. Building conditions that suppress microcracking at the edges of components will also be optimized in the future. This work establishes a unique correlation between laser scanning conditions and microstructural features influencing crack density, leveraging extensive experimental data and predictive regression models. The methodology not only enhances the understanding of microcracking mechanisms but also paves the way for a data-driven approach to optimize additive manufacturing of complex components.

Supplementary data to this article can be found online at https://doi.org/10.1016/j.jmapro.2025.07.023.

CRediT authorship contribution statement

Masahiro Kusano: Writing – original draft, Visualization, Validation, Methodology, Investigation, Formal analysis, Data curation. **Toshio Osada:** Writing – review & editing, Funding acquisition. **Makoto Watanabe:** Writing – original draft, Project administration, Funding acquisition, Conceptualization.

Declaration of competing interest

The authors declare that they have no known competing financial interests or personal relationships that could have appeared to influence the work reported in this paper.

Acknowledgements

This work was partly supported by the Cross-ministerial Strategic Innovation Promotion Program (SIP) “Materials Integration for Revolutionary Design System of Structural Materials” (funding agency: Japan Science and Technology Agency); a JSPS KAKENHI grant (No. 23K13583); and a grant from the Amada Foundation (No. AF-2022201-A3).

References

[1] Adair D, Kirka M, Ryan D. Additive manufacture of prototype turbine blades for hot-fired engine performance validation trials. Proc ASME Turbo Expo 2019;6:1–8. https://doi.org/10.1115/GT2019-90966.
[2] Kou S. Welding Metallurgy. 2003. https://doi.org/10.22486/iwj.v4i3.150243.
[3] Henderson MB, Arrell D, Larsson R, Heobel M, Marchant G. Nickel based superalloy welding practices for industrial gas turbine applications. Sci Technol Weld Join 2004;9:13–21. https://doi.org/10.1179/136217104225017099.
[4] DuPont JN, Lippold JC, Kiser SD. Welding metallurgy and weldability of nickel-base alloys. 2009.
[5] Nagira T, Kitano H, Kimura T, Yoshinaka F, Takamori S, Sawaguchi T, et al. In-situ observation of solidification behaviors of Fe-Mn-Cr-Ni-Si alloy during TIG melt-run welding using synchrotron radiation X-ray. Mater Charact 2024;214:114093.
[6] Norouzian M, Amne Elahi M, Plapper P. A review: suppression of the solidification cracks in the laser welding process by controlling the grain structure and chemical compositions. J Adv Join Process 2023;7:100139.
[7] Kou S. A criterion for cracking during solidification. Acta Mater 2015;88:366–74.
[8] Rappaz M, Drezet JM, Gremaud M. A new hot-tearing criterion. Metal Mater Trans A Phys Metal Mater Sci 1999;30:449–55.
[9] Ghoussoub JN, Tang YT, Dick-Cleland WJB, Németh AAN, Gong Y, McCartney DG, et al. On the influence of alloy composition on the additive manufacturability of Ni-based superalloys. Metall Mater Trans A Phys Metall Mater Sci 2022;53:962–83.
[10] Chandra S, Tan X, Narayan RL, Wang C, Tor SB, Seet G. A generalised hot cracking criterion for nickel-based superalloys additively manufactured by electron beam melting. Addit Manuf 2021;37:101633.
[11] Yang L, Yang J, Han F, Zhang Z, Li Q, Dong Z. Hot cracking susceptibility prediction from quantitative multi-phase field simulations with grain boundary effects. Acta Mater 2023;250:118821.
[12] Zhang Y, Guo B, Jiang M, Li J, Wang Z, Wang L, et al. Mechanism of grain boundary angle on solidification cracking in directed energy deposition Hastelloy X superalloys. Addit Manuf 2024;93:104406.
[13] Zhou W, Tian Y, Tan Q, Qiao S, Luo H, Zhu G, et al. Effect of carbon content on the microstructure, tensile properties and cracking susceptibility of IN738 superalloy processed by laser powder bed fusion. Addit Manuf 2022;58:103016. https://doi.org/10.1016/j.addma.2022.103016.
[14] Hu Y, Yang X kang, Kang W jiang, Ding Y tian, Xu J yu, Zhang H ying. Effect of Zr content on crack formation and mechanical properties of IN738LC processed by selective laser melting. Trans Nonferrous Met Soc China 2021;31:1350–62. https://doi.org/10.1016/S1003-6326(21)65582-6.
[15] Xu J, Ding Y, Gao Y, Wang H, Hu Y, Zhang D. Grain refinement and crack inhibition of hard-to-weld Inconel 738 alloy by altering the scanning strategy during selective laser melting. Mater Des 2021;209:109940. https://doi.org/10.1016/j.matdes.2021.109940.
[16] Hariharan A, Lu L, Risse J, Kostka A, Gault B, Jägle EA, et al. Misorientation-dependent solute enrichment at interfaces and its contribution to defect formation

mechanisms during laser additive manufacturing of superalloys. Phys Rev Mater 2019;3:123602. https://doi.org/10.1103/PhysRevMaterials.3.123602.
[17] Cloots M, Uggowitzer PJ, Wegener K. Investigations on the microstructure and crack formation of IN738LC samples processed by selective laser melting using Gaussian and doughnut profiles. Mater Des 2016;89:770–84. https://doi.org/10.1016/j.matdes.2015.10.027.
[18] Chen Y, Wang W, Ou Y, Li D, Chang H, Wu Y, et al. Effect of high preheating on the microstructure and mechanical properties of high gamma prime Ni-based superalloy manufactured by laser powder bed fusion. J Alloys Compd 2023;960:170598. https://doi.org/10.1016/j.jallcom.2023.170598.
[19] Zhang L, Li Y, Zhang S, Zhang Q. Selective laser melting of IN738 superalloy with a low Mn+Si content: effect of energy input on characteristics of molten pool, metallurgical defects, microstructures and mechanical properties. Mater Sci Eng A 2021;826:141985. https://doi.org/10.1016/j.msea.2021.141985.
[20] Qiu C, Chen H, Liu Q, Yue S, Wang H. On the solidification behaviour and cracking origin of a nickel-based superalloy during selective laser melting. Mater Charact 2019;148:330–44. https://doi.org/10.1016/j.matchar.2018.12.032.
[21] Zhou W, Zhu G, Wang R, Yang C, Tian Y, Zhang L, et al. Inhibition of cracking by grain boundary modification in a non-weldable nickel-based superalloy processed by laser powder bed fusion. Mater Sci Eng A 2020;791:139745. https://doi.org/10.1016/j.msea.2020.139745.
[22] Benoit MJ, Mazur M, Easton MA, Brandt M. Effect of alloy composition and laser powder bed fusion parameters on the defect formation and mechanical properties of Inconel 625. Int J Adv Manuf Technol 2021;114:915–27.
[23] Zhang Y, Cao B, Liu Z, Jiang D, Ye S, Liu T, et al. Inhibiting cracking and improving strength-ductility for laser powder bed fusion René 104 superalloy by Sc and Y microalloying. Mater Sci Eng A Struct Mater 2024;913:147054.
[24] Tomus D, Rometsch PA, Heilmaier M, Wu X. Effect of minor alloying elements on crack-formation characteristics of Hastelloy-X manufactured by selective laser melting. Addit Manuf 2017;16:65–72.
[25] Kitano H, Tsujii M, Kusano M, Yumoto A, Watanabe M. Effect of plastic strain on the solidification cracking of Hastelloy-X in the selective laser melting process. Addit Manuf 2021;37:101742.
[26] Kadoi K, Matsumoto Y, Chiba H, Inoue H. Solidification cracking susceptibility of alloy 718 during additive manufacturing and evaluating method. J Mater Res Technol 2024;33:6389–96.
[27] Wang D, Zhao D, Liang X, Li X, Lin F. Multiple stages of smoking phenomenon in electron beam powder bed fusion process. Addit Manuf 2023;66:103434. https://doi.org/10.1016/j.addma.2023.103434.
[28] Rizza G, Galati M, Iuliano L. A phase-field study of neck growth in electron beam powder bed fusion (EB-PBF) process of Ti6Al4V powders under different processing conditions. Int J Adv Manuf Technol 2022;123:855–73.
[29] Li Y, Liang X, Peng G, Lin F. Effect of heat treatments on the microstructure and mechanical properties of IN738LC prepared by electron beam powder bed fusion. J Alloys Compd 2022;918:165807. https://doi.org/10.1016/j.jallcom.2022.165807.
[30] Kusano M, Takata Y, Yumoto A, Watanabe M. Effects of time per layer and part geometry on thermal history and microcracking in the fabrication of nickel superalloy samples by laser powder bed fusion. Addit Manuf 2024;80:103987.
[31] Wang H, Zhang X, Wang GB, Shen J, Zhang GQ, Li YP, et al. Selective laser melting of the hard-to-weld IN738LC superalloy: efforts to mitigate defects and the resultant microstructural and mechanical properties. J Alloys Compd 2019;807. https://doi.org/10.1016/j.jallcom.2019.151662.
[32] Grange D, Bartout JD, Macquaire B, Colin C. Processing a non-weldable nickel-base superalloy by Selective Laser Melting: role of the shape and size of the melt pools on solidification cracking. Materialia 2020;12. https://doi.org/10.1016/j.mtla.2020.100686.
[33] Jena A, Atabay SE, Brochu M. Microstructure and mechanical properties of crack-free Inconel 738 fabricated by laser powder bed fusion. Mater Sci Eng A 2022;850:143524. https://doi.org/10.1016/j.msea.2022.143524.
[34] Hafezi M, Kermanpur A, Rezaeian A, Saeidirad S, Nikneshan V, Rabieifar H, et al. Investigating crack formation in IN738LC Ni-based superalloy fabricated by laser powder-bed fusion process. J Mater Res Technol 2024;29:1983–2002.
[35] Geiger F, Kunze K, Etter T. Tailoring the texture of IN738LC processed by selective laser melting (SLM) by specific scanning strategies. Mater Sci Eng A 2016;661:240–6. https://doi.org/10.1016/j.msea.2016.03.036.
[36] Lam MC, Lim SCV, Song H, Zhu Y, Wu X, Huang A. Scanning strategy induced cracking and anisotropic weakening in grain texture of additively manufactured superalloys. Addit Manuf 2022;52:102660.
[37] "Fiji: an open-source platform for biological-image analysis" Johannes Schindelin, Ignacio Arganda-Carreras, Erwin Frise, Verena Kaynig, Mark Longair, Tobias Pietzsch, Stephan Preibisch, Curtis Rueden, Stephan Saalfeld, Benjamin Schmid, Jean-Yves Tinevez, Daniel James White, Volker Hartenstein, Kevin Eliceiri, Pavel Tomancak & Albert Cardona.
[38] Tang YT, Panwisawas C, Ghoussoub JN, Gong Y, Clark JWG, Németh AAN, et al. Alloys-by-design: application to new superalloys for additive manufacturing. Acta Mater 2021;202:417–36.
[39] Guo C, Li S, Shi S, Li X, Hu X, Zhu Q, et al. Effect of processing parameters on surface roughness, porosity and cracking of as-built IN738LC parts fabricated by laser powder bed fusion. J Mater Process Technol 2020;285:116788.
[40] Kunze K, Etter T, Grässlin J, Shklover V. Texture, anisotropy in microstructure and mechanical properties of IN738LC alloy processed by selective laser melting (SLM). Mater Sci Eng A 2014;620:213–22.
[41] Chen J, Xu J, Moverare J, Barrales-Mora LA. Effect of the building direction on the high-temperature mechanical properties of an IN738LC superalloy processed by laser-powder bed fusion. Mater Sci Eng A 2024;909:146756.
[42] OpenCV: Hough Line Transform docs.opencv.org (web archive link, 26 October 2024). https://docs.opencv.org/3.4/d6/d10/tutorial_py_houghlines.html (accessed on 26 October 2024).
[43] Pedregosa F, Varoquaux G, Gramfort A, Michel V, Thirion B, Grisel O, et al. Scikit-learn: machine learning in {P}ython. J Mach Learn Res 2011;12:2825–30.
[44] Kusano M, Miyazaki S, Watanabe M, Kishimoto S, Bulgarevich DS, Ono Y, et al. Tensile properties prediction by multiple linear regression analysis for selective laser melted and post heat-treated Ti-6Al-4V with microstructural quantification. Mater Sci Eng A Struct Mater 2020;787:139549.
[45] Catchpole-Smith S, Aboulkhair N, Parry L, Tuck C, Ashcroft IA, Clare A. Fractal scan strategies for selective laser melting of 'unweldable' nickel superalloys. Addit Manuf 2017;15:113–22.
[46] Kou S. Grain refining and cracking during solidification. Metall Mater Trans A 2024;55:4663–75.
[47] Sanchez S, Smith P, Xu Z, Gaspard G, Hyde CJ, Wits WW, et al. Powder bed fusion of nickel-based superalloys: a review. Int J Mach Tools Manuf 2021:165. https://doi.org/10.1016/j.ijmachtools.2021.103729.